

1 The genesis of the giant Dajiangping SEDEX-type pyrite deposit, South
2 China

3

4 Wenhong Johnson Qiu,¹ Mei-Fu Zhou,^{1, †} Xiaochun Li,¹ A.E. Williams-Jones,² and
5 Honglin Yuan³

6

7 ¹ *Department of Earth Sciences, University of Hong Kong, Hong Kong SAR, China*

8 ² *Department of Earth and Planetary Sciences, McGill University, 3450 University
9 Street, Montréal, Québec, Canada*

10 ³ *State Key Laboratory of Continental Dynamics, Department of Geology, Northwest
11 University, Collaborative Innovation Center of Continental Tectonics, Xi'an, China*

12

13 [†] *Corresponding author: e-mail, mfzhou@hku.hk*

14

15 **Abstract**

16 The late Devonian Dajiangping pyrite deposit in South China is a giant sediment-
17 hosted stratiform deposit and contains >200 Mt of pyrite ores with an average grade of
18 30 wt.% S. The orebodies are hosted in carbonaceous siltstone and black shale and
19 consist mainly of laminated pyrite ore. Small euhedral pyrite crystals (*Pyrite 1*) and
20 larger subhedral pyrite crystals (*Pyrite 2*) are the main ore mineral and occur as
21 laminated aggregates of subhedral to euhedral grains. Anhedral pyrite crystals (*Pyrite*
22 *3*) associated with pyrrhotite are present in the host rocks and are interbedded with the
23 ore layers. Mass-balance calculations reveal that the pyrite ores have Al-normalized Ca,
24 Mg, Mn, Si, Na, K and organic carbon contents similar to the host sedimentary rocks,

25 precluding substantial carbonate dissolution and a stratiform replacement origin for the
26 ores.

27 *Pyrite 1* and 2 crystals in the laminated ores have $\delta^{34}\text{S}$ values ranging from -28.7 ‰
28 to 23.6 ‰, and mostly lower than -16 ‰. Such highly negative values indicate that the
29 sulfur in these ores was sourced from bacterially reduced seawater sulfate in an open
30 system. *Pyrite 1* and 2 crystals within a single laminated ore sample have similar $\delta^{34}\text{S}$
31 values. The mostly negative sulfur isotopic composition implies that the pyrite
32 crystallized above to just below the seawater-sediment interface by consuming aliquots
33 of H_2S supplied by bacterial sulfate reduction in sulfate-dominated shallow muds.
34 *Pyrite 3* crystals have mostly positive $\delta^{34}\text{S}$ values, ranging from -3.2 ‰ to 42.8 ‰ with
35 a mean of 5.7 ‰. There are also large ranges of $\delta^{34}\text{S}$ values within a single sample, for
36 example, from 12.1 to 42.8 ‰ in sample YF0204. Such positive and highly
37 heterogeneous $\delta^{34}\text{S}$ values likely resulted from thermochemical sulfate reduction (TSR)
38 and anaerobic oxidation of methane coupled with sulfate reduction (AOM-SR) in a
39 tightly closed system of deep sediments during diagenesis that experienced strong
40 Rayleigh fractionation.

41 We propose that the laminated pyrite ores of the Dajiangping deposit formed by
42 sedimentary exhalation in an anoxic sea water column. Hydrothermal fluids leached Fe
43 from the metamorphic basement underlying the stratiform orebodies, as indicated by

the similar Pb isotopic compositions of the laminated ores and metamorphic basement, and vented onto the sea floor. Mixing of Fe^{2+} from the exhaled metalliferous fluids with H_2S from the ambient anoxic seawater resulted in the precipitation of *Pyrite 1* and 2 crystals above and immediately below the sea floor, respectively, and the formation of laminated ores. This was followed by crystallization of a small proportion of *Pyrite 3* in the pores deep within the sediment pile.

Keywords: SEDEX, syngenetic pyrite, in-situ sulfur and lead isotope analysis, sulfate reduction pathways, mass gains and losses.

Introduction

The Devonian sediment-hosted stratiform Dajiangping deposit in South China is the largest pyrite deposit in the country (Qiu et al., 2018) and contains >200 million tons (Mt) of pyrite ores with an average grade of 30 wt.% S (BGE723BGD, 1965). The orebodies are laminated and extend laterally for over 4.2 km (BGE723BGD, 1965). The Dajiangping deposit, the Hongyan deposit (20 Mt @ 26% S) and the Xiniu deposit (37 Mt @ 20.5% S) are together to form the most important pyrite district in China, accounting for >40% of the pyrite production of the country (Fig. 1) (Editorial Board of The Discovery History of Mineral Deposits of China, 1996).

63 Several preliminary studies of the Dajiangping pyrite deposit have been published
64 in Chinese (Zhang et al., 1992; Zhang et al., 1993; Chen et al., 1998a; Chen et al., 1998b)
65 and most of them have interpreted it to be a sedimentary-exhalative (SEDEX) deposit
66 because of the laminated nature of the ores and the conformable contact between the
67 stratiform orebodies and their host sedimentary rocks (Zhang et al., 1992; Zhang et al.,
68 1993; Pan and Zhang, 1994; Wang et al., 1996; Chen et al., 1998a; Chen et al., 1998b).
69 Owing to the fact that the ores in the eastern part of the deposit are massive, some
70 authors have concluded that they may be epigenetic and have formed from
71 hydrothermal fluids that overprinted the primary SEDEX-type laminated ores (Zhang
72 et al., 1992; Zhang et al., 1993; Zhang et al., 1994). It is noteworthy that similar
73 laminated ores of stratiform sediment-hosted sulfide deposits elsewhere also have been
74 interpreted to have formed by epigenetic hydrothermal replacement of stratiform
75 sedimentary rocks or by sub-seafloor replacement of the host mudstone during
76 diagenesis (Williams, 1978; Eldridge et al., 1993; Almodóvar et al., 1997; Perkins and
77 Bell, 1998; Gadd et al., 2015; Magnall et al., 2016). Previous Pb and Nd isotopic studies
78 of pyrite ores from the Dajiangping deposit have concluded that the metals were derived
79 from the upper crust (Zhang et al., 1993; Chen et al., 1998b). The large range of $\delta^{34}\text{S}$
80 values (-25.5 ‰ to 21.1 ‰) of pyrite separates has been noted and taken to indicate that
81 the sulfur was derived from seawater sulfate by bacterial reduction (BSR) (Zhang et al.,

82 1993).

83 The obvious limitation of sulfur isotope analyses of sulfide separates is that a
84 sample may contain fine-grained sulfide minerals with complex textures in different
85 origins, something that is common in the Dajiangping deposit. High spatial resolution
86 in-situ sulfur isotopic analysis, however, is able to detect the isotopic compositions of
87 individual sulfide grains of different origin (Mason et al., 2006; Kozdon et al., 2010;
88 Ulrich et al., 2011), making it possible to distinguish syngenetic, diagenetic and
89 epigenetic pyrite in finely laminated ores. Owing to the lack of in-situ sulfur isotopic
90 data, the ore forming process of the Dajiangping deposit is still an open question. In
91 addition, the samples analyzed in previous studies were mostly collected randomly
92 from the open pit, as systematic stratigraphic sampling was not possible. Such random
93 sampling made it impossible to evaluate the depositional history of the stratiform
94 orebodies and thus the ore-forming process.

95 In this study, we use high spatial resolution LA-MC-ICP-MS analyses to obtain
96 in-situ sulfur isotopic compositions of pyrite in samples collected systematically from
97 two drill holes, which intersected the four main stratiform orebodies and the
98 immediately adjacent host sedimentary rocks of the Dajiangping deposit. Here, we also
99 report sulfur isotope compositions of pyrite separates, lead isotope compositions of
100 pyrite grains, and major element compositions and organic carbon concentrations of

101 bulk rocks and ores. These new datasets are used to (1) determine if the laminated ores
102 of the stratiform orebodies formed by syn-sedimentary or diagenetic processes or were
103 the result of epigenetic stratiform replacement, (2) determine the sources of metal and
104 sulfur and the sulfate reduction pathways for each type of pyrite, (3) reconstruct the
105 ore-forming process, and (4) compare the distinct sulfur isotopic compositions and
106 sulfate reduction pathways for this pyrite deposit to those of other SEDEX deposits,
107 which are mostly dominated by Pb-Zn sulfides. By integrating these datasets, we have
108 been able to develop a new, well-supported model for the formation of the Dajiangping
109 deposit and the implications for the genesis of other SEDEX-type deposits are also
110 discussed.

111 **Regional geology**

112 The South China Block, in which the Dajiangping deposit is located, comprises
113 the Yangtze Block to the northwest and the Cathaysia Block to the southeast (Fig. 1),
114 which were welded together at ca. 830 Ma (Zhao et al., 2011). The Cathaysia Block
115 consists of a metamorphic basement of Neoproterozoic to Silurian siliciclastic
116 successions and early Paleozoic granites (Zhong et al., 1996; Wan et al., 2010), overlain
117 unconformably by Devonian and younger sedimentary strata.

118 The Cathaysia Block was in a marginal setting in Gondwana during the
119 Neoproterozoic to Silurian, as indicated by the faunal affinity of fossils in the Early

120 Paleozoic shallow marine sedimentary strata of the South China Block to those of
121 northeast Gondwana (Zhao et al., 1996; Metcalfe, 2006). During the early Paleozoic
122 (460–420 Ma), the block was involved in an intracontinental orogeny (Wan et al., 2010;
123 Wang et al., 2013a; Zhang et al., 2017), which was accompanied by upper amphibolite-
124 granulite facies metamorphism and coeval magmatism (Wang et al., 2013b).

125 The South China Block was rifted and separated from Gondwana during the
126 Devonian due to the opening of the Paleo-Tethys Ocean (Metcalfe, 2006). During this
127 period, the South China Block is thought to have been situated along a passive
128 continental margin on the northern side of Palaeo-Tethys (Zhao et al., 1996). This
129 interpretation is supported by the presence of a conspicuous unconformity between pre-
130 Devonian metamorphic basement rocks and Devonian strata, and a subsequent
131 Devonian-Triassic passive margin sequence along the southern margin of the South
132 China Block (Metcalfe, 2006; Zhang et al., 2017). A series of fault-bounded basins,
133 controlled by NNE-SSW and NW-SE trending growth faults, such as the Wuchuan-
134 Sihui deep fault zone (Fig. 1), developed on this passive margin as a result of the rifting
135 and northward drift of the South China Block from Gondwana during the Devonian
136 (Zhao et al., 1996; Chen et al., 2001; Chen et al., 2006; Zhang et al., 2017). Thick
137 sedimentary successions of deep-water facies filled these basins, and as a result of the
138 activation of growth faults, exhalation of hydrothermal fluids led to the formation of

139 chert and numerous SEDEX deposits in the Devonian strata (Fig. 1) (Zhou, 1990; Xu
140 et al., 1996; Zhao et al., 1996; Chen et al., 2006; Gu et al., 2007). The South China
141 Block collided with the Indochina Block during the late Permian-early Triassic, leading
142 to the accretion of the allochthonous continental blocks of Southeast Asia (Metcalf,
143 2006; Qiu et al., 2016; 2017). Pre-Devonian metamorphic rocks and late Paleozoic
144 sedimentary rocks in the Cathaysia Block were reworked by thrust faults, ductile shear
145 zones and granitoid intrusions (Wang et al., 2005).

146 In the southwestern part of the Cathaysia Block, numerous stratiform-stratabound
147 pyrite, Pb-Zn sulfide and barite deposits formed in the Devonian-Carboniferous strata
148 of the fault-bounded basins. These stratiform-stratabound deposits are widespread in
149 basins such as the Qingzhou-Luoding trough of western Guangdong Province (Lai,
150 1996) and the Guizhong Basin of Guangxi Province (Fig. 1) (Chen and Gao, 1987).
151 Strike-slip basins in the Qingzhou-Luoding trough were produced by the deep, NNE
152 trending Wuchuan-Sihui fault (Lai, 1996), whereas those in the Guizhong Basin were
153 controlled by NE-trending transtensional faults (Chen and Gao, 1987) (Fig. 1). The
154 stratiform pyrite deposits occur mainly in the Qingzhou-Luoding trough, and include
155 the giant Dajiangping, and large Hongyan and Xiniu deposits, which are hosted in
156 Devonian carbonaceous elastic and carbonate sedimentary rocks (Pei, 1989; Lai, 1996).
157 The sulfide minerals in these deposits are dominated by pyrite, and include minor

158 proportions of pyrrhotite, galena and sphalerite. The sediment-hosted stratiform nature
159 of these pyrite deposits is similar to that of many SEDEX deposits elsewhere in the
160 world, except that the latter are mostly dominated by Pb-Zn sulfides (Large et al., 2005;
161 Leach et al., 2005; Sangster, 2017). The pyrite deposits, therefore have been interpreted
162 to be SEDEX deposits. They are considered to have formed contemporaneously with
163 sedimentation by exhalation of hydrothermal fluids along basin-bounding growth faults
164 during the Devonian to Carboniferous (Lai, 1996; Yang et al., 1996; Chen et al., 2006).

165 **Deposit geology**

166 The Dajiangping deposit in the northern Qingzhou-Luoding trough, west of the
167 Wuchuang-Sihui fault belt (Fig. 1), comprises stratiform orebodies distributed within a
168 ~6 km long × ~4 km wide zone (Fig. 2). Within the district, there are three contiguous
169 mining centers, namely Jianshan in the south, Dajiangping in the center and
170 Changpailing in the north (Fig. 3). Only orebodies in Dajiangping are currently being
171 mined, with the production coming from a large open pit. A recent Re-Os isochron age
172 of 389 ± 62 Ma for the pyrite ores (Qiu et al., 2018), indicate that the deposit formed
173 in the late Devonian, which is the period assigned to the host strata (see below). The
174 deposit was locally affected by a late Permian-early Triassic orogenic event
175 (BGE723BGD, 1965) that thrust the basement rocks to the east onto the ore-bearing
176 strata along the east-dipping F4 fault, which dips at an angle of 44° to 58° (Figs. 2 and

177 3). In the west, the west-dipping F1 fault (63° to 79°) separates the western basement
178 complex from the eastern ore strata (Fig. 3). An east-dipping normal fault (F3)
179 subdivides the Dajiangping mining district into western and eastern mining areas (Fig.
180 3).

181 The orebodies and host sedimentary layers in the western mining area are weakly
182 deformed and conformable (Figs. 4a and b), and the primary laminated textures of the
183 ores are well preserved (Figs. 4c to f). The stratiform orebodies consist dominantly of
184 intercalated parallel layers of pyrite, chert, black shale and siltstone-sandstone (Figs. 4c
185 to f). In contrast, orebodies in the eastern mining area form an east-dipping syncline
186 that developed due to thrusting along the F4 fault (Fig. 3). These orebodies show
187 evidence of extensive deformation and crystallization to form massive ores (Figs. 4g
188 and h). The primary bedding of ores close to the thrust faults in the eastern mining area
189 has been destroyed and replaced by massive pyrite and shear structures (Figs. 4g and
190 h). Some massive ores were intensely deformed, crosscut by quartz and calcite veins
191 (Fig. 9g) and placed in irregular contact with primary laminated ores (Fig. 9h).

192 ***Host sedimentary rocks***

193 Pyrite orebodies in the Dajiangping deposit are hosted in a carbonaceous
194 sedimentary sequence (Chen et al., 1998a; Chen et al., 1998b). Based on observations
195 of samples from a 550 m deep drill hole, YF02, ~1km to the south of the deposit (Figs.

196 3 and 5), the strata hosting the ores are underlain by a metamorphic basement complex
197 of quartz-mica schist (Figs. 6c and d). The overlying strata, which include the ore strata,
198 are dominated by carbonaceous limestone, siltstone and black shales (Figs. 6a and b).
199 The stratigraphic succession is similar to that of the late Devonian Liujiang group in
200 the Cathaysia Block, which is also unconformably underlain by a Pre-Devonian
201 metamorphic basement (BGMRGD, 1988). This suggests that strata hosting the
202 Dajiangping ores were deposited in the late Devonian, which is the period of ore
203 formation, based on the age of the deposit of 389 ± 62 Ma reported above.

204 The ores are hosted by carbonaceous rocks that have been subdivided into three
205 units. The Lower Unit is 50 m thick and consists of interlayered carbonaceous limestone
206 and siltstone (Fig. 5). The Middle Unit is 30 m thick and consists mainly of
207 carbonaceous limestone with a minor clastic component. There are thin pyrite layers at
208 the top of the unit. The Upper Unit is >100 m thick and is composed of carbonaceous-
209 calcareous siltstone and black shale (Fig. 5). Brachiopod and crinoid fossils are widely
210 distributed in the carbonaceous limestone and are closely associated with organic matter
211 (Figs. 6a and b).

212 ***Stratiform orebodies and mineralized units***

213 The stratiform orebodies of the Dajiangping deposit are conformable with the host
214 clastic carbonaceous strata (Figs. 4a and b), vary in total thickness from 50 to 172 m

215 and extend laterally along a north/south strike for more than 4160 m (Fig. 3)
216 (BGE723BGD, 1965). Based on the lithological changes in drill hole YF04 in the center
217 of the deposit (Fig. 3), the orebodies, which dip shallowly, have thicknesses of up to
218 200 m. They have been divided into four ore units (M1 to M4) (Fig. 5). The lowermost
219 unit (M1), 11 m thick, is the basal unit, lies unconformably on the metamorphic
220 basement and is marked by silicification (Fig. 5). This unit consists of poorly bedded
221 pyrite-pyrrhotite with minor sphalerite in a calcareous-carbonaceous siltstone
222 containing a small proportion of organic matter (Fig. 5). The second unit (M2) is 79 m
223 thick and comprises massive to laminated pyrite ores with black shale interlayers (Fig.
224 5). It is separated from the M1 unit by a thin carbonaceous limestone bed. The third unit
225 (M3) is 36 m thick and consists of pyrite laminae interlayered with black shale and
226 carbonaceous siltstone (Fig. 5). It is separated from the massive ores of M2 by a weakly
227 mineralized black shale layer. The uppermost unit (M4) is 19 m thick, comprises thickly
228 laminated pyrite ores with carbonaceous siltstone (Fig. 5) and is separated from M3 by
229 an unmineralized 35 m thick black shale layer (Fig. 5).

230 ***Ore mineralogy***

231 The pyrite layers are composed of aggregates of subhedral to euhedral pyrite
232 crystals which are cemented by authigenic quartz and calcite (Figs. 7a, b and d). The
233 associated black shale and siltstone layers are composed mainly of diagenetic

234 muscovite and illite, quartz, K-feldspar and calcite with minor pyrite (Figs. 7c and e).
235 Three types of primary pyrite have been recognized on the basis of macro- and micro-
236 textures. The first two types, *Pyrite 1 and 2*, form the laminated ores and are the
237 dominant pyrite types in the ore (Figs. 8a to d), however, *Pyrite 2* is much more
238 abundant than *Pyrite 1* (Figs. 8a to d). In contrast, *Pyrite 3* occurs in irregular patches
239 and commonly in pores and fractures in the weakly mineralized sedimentary rocks,
240 where it is commonly associated with pyrrhotite (Figs. 9a to b). The thick, weakly
241 pyritic sedimentary unit between the M3 and M4 units of drill hole YF04 and the black
242 shales in the Upper Unit of drill hole YF02 contains abundant *Pyrite 3* (Fig. 4).

243 *Pyrite 1* generally occurs as euhedral-subhedral micron-size cubes <10 to 20 μm
244 in diameter and needles (Figs. 8c and d) that are interspersed among detrital grains of
245 quartz and feldspar. Layers containing *Pyrite 1* are commonly intercalated with layers
246 of *Pyrite 2* and quartz-carbonate siltstone layers (Figs. 8a and b). *Pyrite 1* crystals are
247 also present in the layers of *Pyrite 2*.

248 *Pyrite 2* crystals commonly occur as aggregates along the sedimentary bedding
249 and form continuous to semi-continuous pyrite laminae (<1 mm to several mm thick)
250 that are intercalated with non-pyritic sedimentary layers and fine-grained *Pyrite 1* layers
251 (Figs. 8a and b). The crystals range in diameter from 100 μm to >1000 μm and are
252 subhedral in shape (Figs. 8a and d). Locally, *Pyrite 2* crystals occur as overgrowths on

253 *Pyrite 1* crystals (Figs. 8d to f), indicating that they crystallized after *Pyrite 1*. The
254 *Pyrite 2* crystals commonly contain inclusions of detrital quartz and K-feldspar (Figs.
255 8b and c). Quartz and calcite are frequently observed filling the interstices and void
256 space between these euhedral pyrite crystals and display complex intergrowths and
257 comb-like textures (Figs. 7b and d). These features distinguish them from the detrital
258 silicate grains of the clastic sediments, which do not display these textures (Figs. 7c and
259 e). This indicates that the quartz and calcite crystallized slightly after *Pyrite 2* and are
260 of hydrothermal origin.

261 *Pyrite 3* crystals are generally anhedral and, as noted above, form irregular patches
262 commonly with pyrrhotite. Both the pyrite and pyrrhotite are concentrated mainly in
263 interstices among detrital grains, pore spaces and discrete micro-fractures (Figs. 9a and
264 b and 16). The micro-fractures are highly discontinuous, irregularly distributed, parallel
265 to or across sedimentary layers and may have formed by the fracturing of partially
266 unconsolidated muds during diagenesis (Figs. 9a and b and 16). The pyrite and
267 pyrrhotite frequently form irregularly-shaped fine-grained porous aggregates, which
268 contain inclusions of fine clastic silicate grains, and fill pores in the sediment (Figs. 9d
269 to f). The pyrrhotite crystals of this stage may be intergrown with or surround large
270 subhedral *Pyrite 3* grains in the sedimentary layers of the laminated ores (Fig. 9c),
271 indicating that the pyrrhotite formed slightly later than *Pyrite 3*.

272 **Sampling and analytical methods**

273 Ore and sedimentary rock samples were taken at ~2 m intervals from drill holes
274 YF04 and YF02. They show no evidence of deformation and metamorphism, based on
275 field observation and petrographic examination (Fig. 5 to 9). Laminated and massive
276 ores from the open pit were also sampled systematically to provide a coverage from the
277 center to the margin of the Dajiangping deposit. The samples were crushed and
278 powdered for analysis of their bulk composition. Some crushed samples were sieved
279 and panned, and pyrite separates were handpicked under a binocular microscope for
280 sulfur isotope analyses. Polished thin sections were prepared for petrographic
281 examination and in-situ sulfur and lead isotope analyses from a representative suite of
282 samples. The methods for the analyses of the major element compositions, in-situ sulfur
283 and lead isotope ratios and sulfur isotope ratios of the pyrite separates are described in
284 the appendix.

285 **Analytical Results**

286 *Major element and organic carbon concentrations*

287 The major element and organic carbon contents of the laminated pyrite ores and
288 sedimentary rocks from the drill hole YF04 are listed in Table 1 and plotted against
289 depth in Figure 10. The contents of selected elements/oxides of the pyrite ores and black

290 shales from drill hole YF04 and black shales of the Upper Unit from drill hole YF02
291 are also shown in binary plots (Fig. 11; Qiu et al., 2018).

292 As expected, the laminated pyrite ores from drill hole YF04 have high Fe₂O₃ (7.1
293 to 53.3 wt.%) and S contents (4.5 to 41.4 wt.%), whereas weakly mineralized black
294 shales between the M3 and M4 units have much lower Fe₂O₃ (2.4 to 5.0 wt.%) and S
295 contents (0.6 to 2.9 wt.%) (Fig. 10). Almost all the samples have ZnO, PbO and CuO
296 contents <1 wt.% (Fig. 10), reflecting the dominance of pyrite over sphalerite, galena
297 and chalcopyrite. The MnO content increases sharply from the base to the top of the
298 M1 unit (0.04 to 0.16 wt.%), is high in the M2 unit (0.18 to 1.26 wt.%), the M3 unit
299 (0.14 to 0.78 wt.%) and the M4 unit (0.24 to 1.38 wt.%) and is low in the black shale
300 layer (0.06 to 0.18 wt.%) between the M3 and M4 units (Fig. 10). The Al₂O₃ and SiO₂
301 contents range from 1.0 to 18.2 wt.% and 10.1 to 75.5 wt.%, respectively (Fig. 10).
302 Black shale layers, which consist dominantly of quartz and phyllosilicates, including
303 muscovite and illite, generally have much higher Al₂O₃ and SiO₂ concentrations than
304 the laminated ores (Fig. 10). The total organic carbon content (C_{org}) ranges from 0.1 to
305 1.5 wt.% in the mineralized units and is higher in the black shales between the M3 and
306 M4 units, ranging from 1.0 to 2.2 wt.% (Fig. 10). The major element and organic carbon
307 compositions of the black shales of the Upper Unit in the host strata from drill hole
308 YF02 are very similar to those of the black shales between the M3 and M4 units in drill

309 hole YF04 (Fig.11).

310 Not surprisingly, Fe and S display a strong positive correlation ($R^2=0.98$),
311 indicating that the Fe and S are mostly from pyrite crystals. The Al_2O_3 and Fe_2O_3
312 contents of the laminated ores display a negative correlation ($R^2=0.40$), consistent with
313 the fact that the Al_2O_3 content reflects the phyllosilicate mineral content and the Fe_2O_3
314 content reflects the pyrite content (Fig. 11). The black shales from both drill holes have
315 uniformly low Fe_2O_3 and variable Al_2O_3 concentrations (Fig. 11). The strong positive
316 correlation between the TiO_2 and Al_2O_3 concentrations ($R^2=0.82$) of the laminated ores,
317 and black shales from both drill holes, and the high Al_2O_3 and TiO_2 concentrations of
318 the black shales, indicate that the Ti and Al in the ores and host rocks are hosted mainly
319 in detrital minerals (Fig. 11). Similarly, the strong positive correlation of these samples
320 between K_2O and Al_2O_3 contents ($R^2=0.70$) is consistent with the presence of muscovite
321 and illite. The relationship between SiO_2/Al_2O_3 and K_2O/Al_2O_3 shows that significant
322 Si was sourced from a mixture of detrital muscovite (or diagenetic illite) and quartz
323 (Magnall et al., 2015) (Fig. 11). However, the negative correlation between SiO_2/Al_2O_3
324 and TiO_2 implies that much of the silica has a nondetrital origin (Fig. 11). Organic
325 carbon shows a weakly negative correlation with S content and the laminated pyrite
326 ores have organic carbon concentrations lower than that of the black shales (Fig. 11).
327 The C_{org}/Al values of the laminated pyrite ores range from 0.01 to 0.62 (mean=0.12),

328 similar to those of the black shales, which range from 0.06 to 0.45 (mean=0.16) (Fig.
329 11).

330 The gains and losses of elements during formation of the laminated pyrite ores in
331 the major mineralized units (M2, M3 and M4) were evaluated by normalizing the bulk
332 compositions to constant Al₂O₃ and comparing them to those of the black shales in the
333 Upper Unit of the host strata from drill hole YF02, on the assumption that these shales
334 are representative of the unmineralized rock. The normalization was justified by the
335 observation that there is a good linear correlation between Al₂O₃ and TiO₂ (Fig. 11) and,
336 because Ti is almost invariably an immobile element, the same must be true for Al. The
337 calculation made use of the following equation:

338
$$\Delta \text{ Mass} = \frac{C_i^O / C_{Al_2O_3}^O - C_i^B / C_{Al_2O_3}^B}{C_i^B / C_{Al_2O_3}^B} = (C_i^O / C_i^B) * (C_{Al_2O_3}^B / C_{Al_2O_3}^O) - 1,$$

339 where C is concentration, superscript O represents ores, superscript B represents black
340 shale, and subscript i represents a specific element. In Figure 12, we illustrate the
341 percentile changes for some elements in the mineralized units relative to their
342 concentrations in the unmineralized rock. Our results show that pyrite mineralization in
343 each major ore unit of the Dajiangping deposit was accompanied by major additions of
344 Fe, S, Mn, Ca and Ba and minor additions of Na. Minor proportions of Mg and P were
345 added to units M2 and M4 and concentrations of Si, K and organic carbon (C_{org}) were
346 almost unchanged (Fig. 12).

347 ***Lead isotope compositions***

348 *Pyrite 1* and 2 grains and some composite *Pyrite 1-Pyrite 2* grains in laminated
349 ores from the Dajiangping deposit were analyzed at the State Key Laboratory of
350 Continental Dynamics, Northwest University of China for their in-situ lead isotope
351 compositions, which are reported in [Table 2](#) and shown in [Figure 13](#). The results of
352 these analyses show that although there is a relatively large range for each of the ratios,
353 the distribution of the ratios is the same for both types of pyrite. The ranges are 17.976-
354 18.490 for $^{206}\text{Pb}/^{204}\text{Pb}$, 15.600-15.866 for $^{207}\text{Pb}/^{204}\text{Pb}$ and 38.089-39.054 for $^{208}\text{Pb}/^{204}\text{Pb}$
355 ([Fig. 13](#) and [Table 2](#)). The majority of the pyrite grains have Pb isotope ratios similar
356 to those of the metamorphic basement rocks in the Wuchuan-Sihui region ([Fig. 13](#))
357 ([Zhang et al., 1993](#)).

358 ***Sulfur isotope compositions***

359 *In-situ sulfur isotope analyses:* A total of 138 analyses on 37 samples were made
360 at the Northwest University of China ([Table 3](#)) and 39 analyses on 6 samples at the
361 Geological Survey of Finland ([Table 4](#)). Single spots of pyrite grains were ablated at a
362 spatial resolution of 37 to 53 μm . The in-situ S isotopic analyses generally have
363 analytical errors $< 0.2\text{‰}$ ([Table 3](#) and [Table 4](#)). The results from both laboratories are
364 indistinguishable within the analytical error, confirming the reliability of the data.
365 Owing to the large diameter of the laser beam relative to that of individual *Pyrite 1*

366 crystals, the data for *Pyrite 1* were obtained from crystal aggregates. Values of $\delta^{34}\text{S}$ for
367 *Pyrite 1* and 2 crystals (laminated ores) both display wide ranges and vary from -29.2
368 to 17.7 ‰ and from -28.9 to 25.3‰ respectively, with most values being less than -16 ‰
369 (Fig. 17 and Tables 3 and 4). Some *Pyrite 1* and *Pyrite 2* crystals of samples from the
370 open pit and the lowermost ore layers in drill hole YF02 have positive $\delta^{34}\text{S}$ values. The
371 in-situ analyses show that the $\delta^{34}\text{S}$ values for both *Pyrite 1* and *Pyrite 2* crystals within
372 individual laminae vary over a very narrow range (<2 ‰) (Figs. 14 and 15 and Tables
373 3 and 4). Values of $\delta^{34}\text{S}$ for *Pyrite 3* (in-situ analyses) in the black shales are mainly
374 positive (-1.5 ‰ to 42.9 ‰), with most values being > 3 ‰ (Table 3). They vary
375 considerably within a single sample (Figs. 16a to f), e.g., from -0.5 ‰ to 5.6 ‰ in
376 YF0409, 12.1 ‰ to 42.8 ‰ in YF0204, and -1.5 ‰ to 25.2 ‰ in YF0205.

377 *Sulfur isotope compositions of pyrite separates:* Given that the laminated ores have
378 a relatively homogenous sulfur isotope composition on the scale of individual laminae,
379 pyrite separates of 33 laminated ores from drill hole YF04 and pyrite separates of 33
380 laminated and massive ores from the open pit were analyzed. These separates have $\delta^{34}\text{S}$
381 values from -28.7 ‰ to 19.0 ‰ (Table 5), consistent with the range obtained with in-
382 situ analysis. Pyrite separates of laminated ores from the mineralized units in drill hole
383 YF04 yielded negative $\delta^{34}\text{S}$ values, ranging from -28.2 ‰ to -1.8 ‰, whereas some
384 samples collected from the open pit yielded positive $\delta^{34}\text{S}$ values (Table 5). In Figure 16,

the isotopic data of pyrite separates are combined with the in-situ isotopic data for *Pyrite 1, 2 and 3* in a histogram that compares the $\delta^{34}\text{S}$ values of *Pyrite 1 and 2* from the laminated ores with those for *Pyrite 3* from the host rocks. From this diagram, it is evident that the $\delta^{34}\text{S}$ values for the pyrite of the laminated ores (*Pyrite 1* and *2*) are mostly negative ($< -16\text{‰}$), ranging from -28.7 to 23.8‰ , whereas those for *Pyrite 3* in the black shales are mostly positive ($> 3\text{‰}$), ranging from -1.5‰ to 42.9‰ (Fig. 17).

Discussion

Environment of ore deposition

The stratiform nature of the orebodies and the sulfide lamination are essential features of the Dajiangping deposit. Such features are commonly taken as evidence for the sedimentary-exhalative (SEDEX) origin of deposits of this type, although these deposits are generally dominated by galena and sphalerite rather than pyrite (Large et al., 1998; Leach et al., 2005). According to the SEDEX model, exhalative metalliferous fluids mix with anoxic H_2S -rich seawater, leading to crystallization of sulfide particles in the water column along an interface between these two fluids, followed by gravitational deposition of the sulfide aggregates to the basin floor to develop the characteristic laminated sulfide textures (Large et al., 1998; Large et al., 2005). A number of studies, however, have proposed that the sulfide minerals of laminated ores crystallize within both the shallow sulfate-rich zone and deep sulfate-depleted zone of

404 muds below the sediment-water interface of brine pools on the sea floor, and that the
405 required H₂S is produced within the sediments by bacterial reduction of the infiltrating
406 seawater sulfate (Sangster, 2002; Ireland et al., 2004; Sangster, 2017). Laminated
407 sulfide ores also have been interpreted to form by replacement of the host strata, a
408 hypothesis that is supported by the observation that sulfide mineral deposition involves
409 acid generation (e.g., $\text{Fe}^{2+} + 2\text{H}_2\text{S} = \text{FeS}_2 + 4\text{H}^+$), which promotes carbonate mineral and
410 organic carbon dissolution and enhances porosity, thereby facilitating lateral fluid
411 migration.(Eldridge et al., 1993; Hinman, 1996; Perkins and Bell, 1998; Chen et al.,
412 2003). For example, Perkins and Bell (1998) proposed that laminated sulfide ores in the
413 stratiform orebodies of the McArthur River (HYC) deposit formed by replacement of
414 carbonate and bituminous beds. Similarly, Eldridge et al. (1993) proposed that the
415 laminated sulfide ores of the Mount Isa and Hilton deposits formed by replacement of
416 dolomite. In the following paragraphs, we test these hypotheses for the Dajiangping
417 deposit using the observations and data that have been presented in this paper.

418 As reported earlier, much of the pyrite in the stratified ores of the Dajiangping
419 deposit occurs as small euhedral to subhedral pyrite cubes (*Pyrite 1*) measuring <10 to
420 20 µm in diameter. This observation clearly rules out the replacement model, which
421 would predict the formation of dominantly anhedral pyrite resulting from the alteration
422 of precursor minerals or the filling of voids. Furthermore, the fact that *Pyrite 1* and

423 *Pyrite 2* grains are partly cemented by calcite (Fig. 7b2) and there was no loss of
424 carbonate-associated elements (e.g., Ca, Mg and Mn) and organic matter (C_{org}) (Fig. 12)
425 is inconsistent with carbonate and bituminous dissolution.

426 A process that could explain the small size and cubic morphology of the *Pyrite 1*
427 crystals is direct precipitation from a mixture of vent fluid and seawater. In this respect,
428 it is noteworthy that Feely et al. (1987,1990) has described smoker particulates from
429 active vents on the Juan de Fuca Ridge, in which the pyrite occurs as euhedral cubes
430 ranging in diameter from $\sim 0.1 \mu m$ to tens and in some cases hundreds of microns. It is
431 thus reasonable to propose that the *Pyrite 1* crystals, which have diameters within this
432 range, settled under gravity from a mixed hydrothermal fluid-seawater column to form
433 the observed laminae at the sediment-seawater interface.

434 The origin of *Pyrite 2* is less obvious. As reported earlier, it enclosed and formed
435 overgrowths on *Pyrite 1* indicating that it formed later. For one of the reasons given for
436 eliminating the replacement model for *Pyrite 1*, namely the lack of evidence of
437 carbonate and bituminous dissolution, we can also eliminate this model for *Pyrite 2*,
438 which is commonly cemented by calcite and quartz. Given its clearly secondary origin,
439 we therefore propose that *Pyrite 2* formed by growing on *Pyrite 1* crystals in relatively
440 shallow muds below the sediment-seawater interface. The laminated nature (Figs.4c to
441 f, Fig.5) and minor detrital content of some *Pyrite 2* dominated massive ores (Fig. 4e)

indicate that they were unlikely to have crystallized in deep muds well below the sediment-water interface because, if this were the case, there would have been a very much higher proportion of detrital material in the ores.

In contrast to *Pyrite 1* and 2, *Pyrite 3* and pyrrhotite crystals, based on their anhedral shapes, and occurrence in voids between clasts (Figs. 9a to f), likely crystallized deeper in the sediment column during diagenesis. Some *Pyrite 3* and pyrrhotite crystals occur in micro-fractures within sediment layers (Figs. 9a and b), which likely formed due to compaction when the sediment was partially consolidated, which is also consistent with a diagenetic origin for *Pyrite 3* and pyrrhotite.

Source of reduced sulfur

In spite of the different modes of $\delta^{34}\text{S}$ values for each pyrite type (Fig. 17), the maximum $\delta^{34}\text{S}$ values are very similar and strongly positive ($\sim 24\text{‰}$), suggesting that the sulfur of the three types of pyrite in the Dajiangping deposit had the same source, namely sea water sulfate (Seal, 2006). In order to reliably estimate the $\delta^{34}\text{S}$ value of the source from the data for pyrite, it is necessary to know the temperature of pyrite deposition. Owing to a lack of fluid inclusions suitable for microthermometric analysis and a lack of mineral pairs suitable for stable isotope geothermometry, we assume that the Dajiangping deposit formed at a temperature comparable to that of SEDEX deposits elsewhere, i.e., 150°C to 270°C (Cooke et al., 2000). For these temperatures, the sulfur

461 isotope fractionation between pyrite and H₂S ($\epsilon^{34}\text{S}_{\text{Pyrite-H}_2\text{S}}$) is 2‰ and 1‰, respectively,
462 and even at 10 °C is only 5‰ (Seal, 2006). Based on this fractionation, the maximum
463 $\delta^{34}\text{S}$ value analysed for pyrite would correspond to a $\delta^{34}\text{S}$ value of H₂S in the
464 mineralizing fluid of ~19‰ at 10°C or 23‰ at 270°C. Significantly, the $\delta^{34}\text{S}$ value of
465 sea water for the late Devonian-early Carboniferous is estimated to have been 23‰
466 (Claypool et al., 1980; Kampschulte and Strauss, 2004; Bottrell and Newton, 2006). We
467 therefore conclude that the sulfur for the Dajiangping deposit was sourced from coeval
468 seawater sulfate, a conclusion that has been drawn for most other stratiform sediment-
469 hosted Zn-Pb-(Cu-Ag-Ba) deposits (Leach et al., 2005).

470 Sulfate reduction pathways

471 Although seawater sulfate is ultimately the source for sulfur in the sulfide minerals
472 of most SEDEX deposits and sedimentary rocks (Leach et al., 2005; Rajabi et al., 2014),
473 the sulfate reduction pathways may be different as will be the resulting sulfur isotope
474 signatures. Bacterial sulfate reduction (BSR) will lead to very negative $\delta^{34}\text{S}$ values, as
475 was the case for syn-sedimentary framboidal pyrite in the Howard's Pass SEDEX Zn-
476 Pb deposit (-16.6 ‰ on average), whereas thermochemical sulfate reduction, which
477 might occur during diagenesis will produce very positive values (Gadd et al., 2016).
478 Sulfate reduction coupled with anaerobic oxidation of methane (SR-AOM) which
479 occurs in the sulfate-methane transition zone (SMTZ) during diagenesis, would also

480 produce H₂S with very positive $\delta^{34}\text{S}$ values (Borowski et al., 2013; Magnall et al., 2016;
481 Fernandes et al., 2017). The reason for such different sulfur isotope signatures is that at
482 the very low temperature of BSR the fractionation between sulfate and H₂S is very high,
483 it can reach 70 ‰ at the temperature of seawater on the ocean floor (Canfield, 2001;
484 Canfield et al., 2010; Sim et al., 2011; Wing and Halevy, 2014), whereas at the
485 temperatures required for thermochemical sulfate reduction (TSR), it is very low,
486 e.g., 15 ‰ at 150°C (Seal, 2006). The positive $\delta^{34}\text{S}$ values of H₂S during SR-AOM are
487 due to the rapid reduction of infiltrated sulfate in sediment pores and strong Rayleigh
488 fractionation of sulfur isotopes during the oxidation of methane (Borowski et al., 2013;
489 Magnall et al., 2016; Fernandes et al., 2017).

490 *Pyrite 1* and 2 crystals generally have $\delta^{34}\text{S}$ values between -16 and -30 ‰, although
491 a small proportion of crystals have values > +20 ‰. This indicates that most of the
492 sulfur in *Pyrite 1 and 2* originated by bacterial sulfate reduction. Such negative $\delta^{34}\text{S}$
493 values (<-16 ‰), even with BSR, however, would have required an open system with
494 an unlimited supply of seawater sulfate, e.g., within a seawater column above the
495 seawater-sediment interface in a restricted marine basin, like that of the modern Black
496 Sea (Lyons, 1997; Neretin et al., 2003). The observation that the $\delta^{34}\text{S}$ values of
497 individual pyrite ore laminae (*Pyrite 1* and 2) vary within a very small range is
498 consistent with this conclusion (Fig. 14, Fig. 15 and Tables. 3 and 4). In contrast, as

499 *Pyrite 3* appears to have crystallized in sediment pores during diagenesis, its high $\delta^{34}\text{S}$
500 likely resulted from either TSR or SR-AOM in response to a high geothermal gradient
501 or hydrothermal activity.

502 **The genesis of *Pyrite 1 and 2***

503 As discussed above, the available evidence indicates that the micron-sized *Pyrite*
504 *1* cubes formed in the seawater column. We consider that this occurred rapidly (thereby
505 explaining the small size of the crystals) when a hot, iron-rich fluid mixed with cold
506 seawater containing H_2S that was being produced by bacterial reduction of sulfate. In
507 contrast, the much larger *Pyrite 2* crystals that enclose and overgrew *Pyrite 1* crystals
508 are interpreted to have formed later and much more slowly beneath the sediment-
509 seawater interface. This pyrite preserved the laminar distribution of *Pyrite 1* effectively
510 and replaced *Pyrite 1* to form coarse-grained laminae that are intercalated with the
511 *Pyrite 1* laminae. We therefore conclude that *Pyrite 1 and 2* formed syngenetically in
512 the water column and below the sediment-seawater interface, respectively.

513 The strongly negative $\delta^{34}\text{S}$ values of the bulk of the *Pyrite 1 and 2* crystals in the
514 Dajiangping deposit contrast with the predominantly positive $\delta^{34}\text{S}$ values of the major
515 sulfide minerals in most distal-type SEDEX Pb-Zn deposits with laminated ores.
516 Whereas the former can be explained simply by BSR, the latter require more convoluted
517 explanations. These explanations include strong Rayleigh fractionation by BSR, TSR

518 or anaerobic oxidation of methane (AOM) within closed or partly closed local
519 reservoirs, e.g., pores beneath the seawater-sediment interface (Lyons et al., 2006;
520 Magnall et al., 2016; Fernandes et al., 2017; Sangster, 2017) or euxinic water columns
521 in restricted basins where sulfate is quantitatively consumed by sulfide formation
522 (Goodfellow, 1987; Goodfellow and Lydon, 2007).

523 As shown in Figures 14 and 15, the very homogenous $\delta^{34}\text{S}$ values of *Pyrite 1 and*
524 *2* in individual laminae referred to above also indicate that these pyrite derived H_2S
525 from sea water, in which the sulfur isotope of H_2S are stable, like those in the modern
526 Black Sea (Neretin et al., 2003). Such feature contrast with the sulfur isotopic behavior
527 in Pb-Zn SEDEX deposits where there is considerable $\delta^{34}\text{S}$ fractionation among the
528 major sulfide minerals on a very small scale, e.g., at HYC, Howard's Pass and Tom-
529 Jason (Eldridge et al., 1993; Ireland et al., 2004; Gadd et al., 2016; Magnall et al., 2016;
530 Sangster, 2017). Importantly for the present study, this behavior is interpreted to reflect
531 sulfide mineralization in a thick sediment column in a relatively closed system, where
532 sulfate supply from the seawater column is slow and seawater sulfate in the pore fluids
533 is quantitatively reduced by BSR, TSR or anaerobic oxidation of methane (AOM).
534 These observations provide compelling evidence that the laminated ores of the
535 Dajiangping deposit could not have formed diagenetically in a deep sediment column
536 or epigenetically.

537 Although the $\delta^{34}\text{S}$ values of the *Pyrite 1 and 2* crystals are mostly negative, some
538 of these crystals also have positive values. The latter *Pyrite 1 and 2* crystals are
539 indistinguishable from those with strongly negative $\delta^{34}\text{S}$ values, indicating that they
540 formed in the same environments (above and below the seawater-sediment interface,
541 respectively) and therefore were also the products of BSR. The reason for these high
542 $\delta^{34}\text{S}$ values is unclear. They may have resulted, however, from local disequilibrium
543 (sulfate supply < sulfate consumption), addition of toxins to the bacteria, or locally high
544 temperature in the water column due incomplete mixing of the seawater with the
545 hydrothermal fluid leading to TSR instead of BSR (Sangster, 2017).

546 Organic matter is essential to maintain the anoxic conditions on the sea floor
547 required for BSR and is also the main electron donor for sulfate (electron acceptor)
548 reduction. The similar $\text{C}_{\text{org}}/\text{Al}$ values of the laminated pyrite ores and black shales
549 indicate that primary productivity in the water column was high and stable during both
550 the ore-forming and non-ore forming stages (Fig. 11), thereby ensuring that there was
551 sufficient stable organic matter accumulation on the sea floor for the BSR required to
552 crystallize large amounts of *Pyrite 1 and 2*. The abundance of micro-fossils (Figs. 6a
553 and b) in the carbonaceous limestone of the host strata at the margin of deposit, shows
554 that there was a high level of micro-organism activity in the shallow part of the basin
555 (Fig. 5). It is therefore possible that decomposition of these shelly animals may have

introduced abundant organic matter to the sediments, thereby providing the nutrients for BSR.

The genesis of *Pyrite 3*

The distribution of *Pyrite 3* in the interstices among detrital grains, pores in sedimentary layers and fractures of probable diagenetic origin (Fig. 9), suggest that crystallization of *Pyrite 3* occurred during diagenesis. The mostly positive $\delta^{34}\text{S}$ values (-1.5 ‰ to 42.8 ‰; on average 5.7 ‰) of the *Pyrite 3* crystals (Fig. 17) and the lack of highly negative $\delta^{34}\text{S}$ values suggest that sulfur of this pyrite was reduced from sea water sulfate by TSR. Assuming that the initial $\delta^{34}\text{S}_{\text{sulfate}}$ value of sea water sulfate in the pores was approximately ~21‰, as discussed above, the $\delta^{34}\text{S}$ values of *Pyrite 3* can be explained satisfactorily by $\epsilon^{34}\text{S}_{\text{SO}_4\text{-H}_2\text{S}}$ values of TSR <20 ‰ at 100 °C (Machel, 2001), a temperature that is reasonable for diagenesis. The extremely positive $\delta^{34}\text{S}$ values, e.g., 42.8 ‰ in YF0204, for *Pyrite 3* also imply that anaerobic oxidation of methane (AOM) was likely involved in the sulfate reduction (Borowski et al., 2013; Magnall et al., 2016; Fernandes et al., 2017). The high variability of the $\delta^{34}\text{S}$ values of the diagenetic pyrite, even at the scale of a single thin section (Fig. 16), is evidence of extensive Rayleigh fractionation of sulfur isotopes during TSR or AOM in a very tightly closed system. It therefore follows that *Pyrite 3* must have crystallized in a relatively deep part of the sediment pile well beneath the sediment-water interface during but more likely after

575 formation of the laminated ores.

576 **An integrated model for the genesis of the Dajiangping deposit**

577 Recent studies of the genesis of stratiform sediment-hosted sulfide deposits (Zn-
578 Pb deposits) have favored diagenetic models over the original syn-sedimentary-
579 exhalative (brine pool) model, even for the pre-ore pyrite. For example, [Magnall et al.](#)
580 [\(2016\)](#) concluded that pre-ore pyrite in the Tom-Jason Pb-Zn-Ba deposit formed
581 diagenetically in the sulfate-methane transition zone (SMTZ) of the sediments, with the
582 H₂S being derived from reduction of sulfate in pore fluids by anaerobic oxidation of
583 methane (AOM) and the iron being sourced from Fe²⁺ produced by the breakdown of
584 Fe-bearing minerals during diagenesis. It is difficult, however, to envisage such a
585 process producing the large tonnage (>200Mt) and high ore grade (52 wt.% Fe and 30
586 wt.% S) of the Dajiangping deposit, given the very low content of iron in the
587 surrounding black shales ([Fig.10](#)). Moreover, as has already been discussed, pyrite
588 formed in the SMTZ by AOM would be characterized by positive $\delta^{34}\text{S}$ values close to
589 or higher than those of sea water sulfate ([Magnall et al., 2016](#); [Fernandes et al., 2017](#);
590 [Lin et al., 2017](#)), which is not the case for the Dajiangping ores (strongly negative; see
591 above). In a variation of the diagenetic model, [Gadd et al. \(2015, 2016\)](#) proposed that
592 pyrite, sphalerite and other sulfide minerals of the main mineralization stage in the
593 Howard's Pass SEDEX Zn-Pb district crystallized in the pores of sediments, when

594 downwardly diffusing metal ions from a dense brine pool interacted with upwardly
595 diffusing H₂S reduced by TSR. The sulfide minerals in this deposit are also
596 characterized by positive $\delta^{34}\text{S}$ values, interpreted to have resulted from thermal
597 reduction of seawater sulfate in the pore fluids (TSR) in a closed system (Gadd et al.
598 2015; 2016). This model, too, is not applicable to the Dajiangping deposit because of
599 the strongly negative $\delta^{34}\text{S}$ values of the ores.

600 Fluid inclusion analyses and analyses of basinal brines have established that the
601 fluids responsible for metal transport in SEDEX Pb-Zn deposits have relatively high
602 salinity (6 to 20 wt.% NaCl equivalent) (Cooke et al., 2000; Sangster, 2002; Leach et
603 al., 2004). These metalliferous brines are vented at the seafloor and, depending on the
604 discharge rate, will either form a column that mixes with the overlying seawater (higher
605 temperature and higher discharge rate) or flow away from the vents as bottom-hugging
606 fluids and/or collect in depressions on the sea floor to form brine pools (lower
607 temperature and lower discharge rate). We propose that the former was the case for
608 Dajiangping deposit and that the predominantly syngenetic pyrite in this deposit
609 crystallized in a plume above the sediment-water interface, which mushroomed out and
610 mixed fully with ambient sea water, as observed for modern black smokers (Turner and
611 Campbell, 1987; Sangster, 2017). We further propose that the iron was transported as
612 FeCl⁺ (Heinrich and Seward, 1990) and deposited as pyrite in a mixed seawater-brine

613 column with unlimited access to seawater sulfate, when it interacted with isotopically
614 light reduced sulfur produced by BSR.

615 A genetic model is illustrated in Figure 18 and satisfactorily explains the formation
616 of the Dajiangping deposit. According to this model, iron was introduced along a
617 growth fault bounding a basin that developed as a result of rifting during the northward
618 drifting of the South China Block from Gondwana. The source of the iron, based on the
619 Pb isotopic composition of *Pyrite 1* and 2, was the metamorphic basement (Zhang et
620 al., 1993; Chen et al., 1998b) (Fig. 13) and the agent of its transport was a hot brine,
621 which likely reached high temperature due to a relatively steep geothermal gradient
622 (Large et al., 2002; Leach et al., 2005). Syngenetic *Pyrite 1* crystallized when the
623 metalliferous (FeCl⁺-rich) brine vented through the sea floor and mixed with anoxic
624 organic-rich bottom seawater in which the sulfate had undergone bacterial reduction to
625 H₂S (Figs. 18a and b). After fully mixing with the euxinic seawater, the metalliferous
626 brine became less buoyant and descended to the sea floor, where it began infiltrating
627 the underlying sediment. Pyrite was then able to crystallize slowly by surface-
628 controlled processes as coarse-grained pyrite (*Pyrite 2*) in a lower thermal gradient at
629 and below the sea floor, overgrowing and encompassing the accumulated *Pyrite 1* (Fig.
630 18b). Each pulse of hot metalliferous brine exhalation would have resulted in rapid
631 crystallization of *Pyrite 1* from ascending hot metalliferous fluids, forming fine-grained

pyrite layers, followed by subsequent crystallization of *Pyrite 2* in shallow muds to form coarser-grained layers (Fig. 18b). As the H₂S in the seawater column was well mixed and had a homogenous sulfur isotopic composition, *Pyrite 1 and 2*, having both precipitated through interacting with H₂S during the same exhalation, had the same sulfur isotopic composition. *Pyrite 3* crystallized diagenetically in pore spaces and diagenetic fractures in the sediment column, through the interaction of Fe-bearing fluids with sulfur reduced from infiltrated seawater sulfate by TSR and AOM (Fig. 18c). As temperature increased due to increasing sediment deposition or the redox condition became more reducing due to oxidation of organic matter in the deep sediments during diagenesis, pyrrhotite also crystallized in the pores (Fig. 18c).

Conclusions

The Dajiangping sediment-hosted pyrite deposit, which is the largest pyrite deposit in China, comprises stratiform orebodies with finely laminated ores similar to those of many SEDEX deposits. It differs from most SEDEX deposits, however, in that the ores have strongly negative $\delta^{34}\text{S}$ values, reflecting bacterial sulfate reduction of seawater sulfate in a completely open system. A model is proposed, in which the finely laminated ores represent the rapid crystallization of pyrite in a thoroughly mixed metalliferous vent fluid-seawater column containing abundant bacterially reduced sulfur (H₂S). In this model, each pulse of vent fluid-seawater mixture is marked by a waning stage in

651 which the column loses buoyancy and descends to the seafloor, infiltrating the
652 underlying sediment to form coarser-grained intercalated pyrite layers through
653 replacement of the preceding fine-grained pyrite layers. Minor proportions of pyrite
654 formed in the pores of the sediment pile during diagenesis as a result of ongoing
655 downward diffusion of seawater sulfate and its conversion to H₂S by TSR and AOM.

656 **Acknowledgements**

657 This study was supported by a grant from the National Natural Science Foundation
658 of China (41772087) and the Research Grant Council of Hong Kong (17306814). We
659 would like to express our thanks to the geologists of the Yunfu Guangye Pyrite Group
660 Limited, especially Junqiao Tu and Yicheng Wang for their help during our field trip to
661 the Dajiangping deposit. Thanks are also extended to Lu Chen and Zhian Bao of the
662 State Key Laboratory of Continental Dynamics, Department of Geology, Northwest
663 University and Wei Terry Chen from the Institute of Geochemistry, Chinese Academy
664 of Sciences for their assistance with the in-situ sulfur isotope analyses. The manuscript
665 benefited from a review of an early version by John Malpas and was further improved
666 significantly as a result of the comments of two anonymous reviewers and associate
667 editor, Sarah Gleeson.

668

669

REFERENCES

- Almodóvar, G. R., Sáez, R., Pons, J. M., Maestre, A., Toscano, M., and Pascual, E., 1997, Geology and genesis of the Aznalcóllar massive sulphide deposits, Iberian Pyrite Belt, Spain: *Mineralium Deposita*, v. 33, no. 1, p. 111-136.
- Bao, Z., Chen, L., Zong, C., Yuan, H., Chen, K., and Dai, M., 2017, Development of pressed sulfide powder tablets for in situ sulfur and lead isotope measurement using LA-MC-ICP-MS: *International Journal of Mass Spectrometry*, v. 421, p. 255-262.
- BGE723BGD, 1965, Detailed exploration report of Dajiangping prite deposit, Yunfu., 44 p. (in Chinese with English abstract).
- BGMRGD, 1988, Regional Geology of Guangxdong province, Geological Publishing House, Beijing (in Chinese with English abstract).
- Borowski, W. S., Rodriguez, N. M., Paull, C. K., and Ussler, W., 2013, Are ^{34}S -enriched authigenic sulfide minerals a proxy for elevated methane flux and gas hydrates in the geologic record?: *Marine and Petroleum Geology*, v. 43, p. 381-395.
- Bottrell, S. H., and Newton, R. J., 2006, Reconstruction of changes in global sulfur cycling from marine sulfate isotopes: *Earth-Science Reviews*, v. 75, no. 1–4, p. 59-83.
- Canfield, D., 2001, Biogeochemistry of sulfur isotopes: *Reviews in Mineralogy and Geochemistry*, v. 43, no. 1, p. 607-636.
- Canfield, D. E., Farquhar, J., and Zerkle, A. L., 2010, High isotope fractionations during sulfate reduction in a low-sulfate euxinic ocean analog: *Geology*, v. 38, no. 5, p. 415-418.
- Chen, D., Chen, G., Pan, J., Ma, S., Dong, W., Gao, J., and Chen, X., 1998a, Characteristics of the hydrothermal sedimentation of the Dajiangping superlarge pyrite deposit in Yunfu, Guangdong: *Geochimica*, v. 27, no. 1, p. 12-19. (in Chinese with English abstract).
- Chen, D., Ma, S., Dong, W., Chen, X., Chen, G., and Gao, J., 1998b, Pb and Nd isotopes of the Dajiangping pyrite deposit, Guangdong province, and its' metallic ore source: *Mineral Deposits*, v. 17, no. 3, p. 215-223. (in Chinese with English abstract).
- Chen, D., Qing, H., Yan, X., and Li, H., 2006, Hydrothermal venting and basin evolution (Devonian, South China): Constraints from rare earth element geochemistry of chert: *Sedimentary Geology*, v. 183, no. 3, p. 203-216.
- Chen, D., Tucker, M. E., Jiang, M., and Zhu, J., 2001, Long-distance correlation between tectonic-controlled, isolated carbonate platforms by cyclostratigraphy

- and sequence stratigraphy in the Devonian of South China: *Sedimentology*, v. 48, no. 1, p. 57-78.
- Chen, J., Walter, M. R., Logan, G. A., Hinman, M. C., and Summons, R. E., 2003, The Paleoproterozoic McArthur River (HYC) Pb/Zn/Ag deposit of northern Australia: organic geochemistry and ore genesis: *Earth and Planetary Science Letters*, v. 210, no. 3, p. 467-479.
- Chen, L., Chen, K., Bao, Z., Liang, P., Sun, T., and Yuan, H., 2017, Preparation of standards for in situ sulfur isotope measurement in sulfides using femtosecond laser ablation MC-ICP-MS: *Journal of Analytical Atomic Spectrometry*, v. 32, no. 1, p. 107-116.
- Chen, X., and Gao, J., 1987, Thermal water sedimentation and Pb-Zn-Barite deposits: *Acta Sedimentologica Sinica*, v. 5, no. 3, p. 149-158. (in Chinese with English abstract).
- Claypool, G. E., Holser, W. T., Kaplan, I. R., Sakai, H., and Zak, I., 1980, The age curves of sulfur and oxygen isotopes in marine sulfate and their mutual interpretation: *Chemical Geology*, v. 28, p. 199-260.
- Cooke, D. R., Bull, S. W., Large, R. R., and McGoldrick, P. J., 2000, The importance of oxidized brines for the formation of Australian proterozoic stratiform sediment-hosted Pb-Zn (SEDEX) deposits: *Economic Geology and the Bulletin of the Society of Economic Geologists*, v. 95, no. 1, p. 1-17.
- Eldridge, C., Williams, N., and Walshe, J. L., 1993, Sulfur isotope variability in sediment-hosted massive sulfide deposits as determined using the ion microprobe SHRIMP: II. A study of the HYC Deposit at McArthur River, Northern Territory, Australia: *Economic Geology*, v. 88, no. 1, p. 1-26.
- Fernandes, N. A., Gleeson, S. A., Magnall, J. M., Creaser, R. A., Martel, E., Fischer, B. J., and Sharp, R., 2017, The origin of Late Devonian (Frasnian) stratiform and stratabound mudstone-hosted barite in the Selwyn Basin, Northwest Territories, Canada: *Marine and Petroleum Geology*, v. 85, p. 1-15.
- Gadd, M. G., Layton-Matthews, D., Peter, J. M., Paradis, S., and Jonasson, I. R., 2016, The world-class Howard's Pass SEDEX Zn-Pb district, Selwyn Basin, Yukon. Part II: the roles of thermochemical and bacterial sulfate reduction in metal fixation: *Mineralium Deposita*, v. 52, no. 3, p. 1-15.
- Gadd, M. G., Layton-Matthews, D., Peter, J. M., and Paradis, S. J., 2015, The world-class Howard's Pass SEDEX Zn-Pb district, Selwyn Basin, Yukon. Part I: trace element compositions of pyrite record input of hydrothermal, diagenetic, and metamorphic fluids to mineralization: *Mineralium Deposita*, v. 51, no. 3, p. 1-24.
- Gilbert, S. E., Danyushevsky, L. V., Rodemann, T., Shimizu, N., Gurenko, A., Meffre,

- 745 S., Thomas, H., Large, R. R., and Death, D., 2014, Optimisation of laser
746 parameters for the analysis of sulphur isotopes in sulphide minerals by laser
747 ablation ICP-MS: *Journal of Analytical Atomic Spectrometry*, v. 29, no. 6, p.
748 1042-1051.
- 749 Goodfellow, W. D., 1987, Anoxic stratified oceans as a source of sulphur in sediment-
750 hosted stratiform Zn-Pb deposits (Selwyn Basin, Yukon, Canada): *Chemical*
751 *Geology: Isotope Geoscience section*, v. 65, no. 3, p. 359-382.
- 752 Goodfellow, W. D., and Lydon, J. W., 2007, Sedimentary exhalative (SEDEX)
753 deposits: *Mineral deposits of Canada: A synthesis of major deposit types,*
754 *district metallogeny, the evolution of geological provinces, and exploration*
755 *methods: Geological Association of Canada, Mineral Deposits Division,*
756 *Special Publication*, no. 5, p. 163-183.
- 757 Gu, L., Khin, Z., Hu, W., Zhang, K., Ni, P., He, J., Xu, Y., Lu, J., and Lin, C., 2007,
758 Distinctive features of Late Palaeozoic massive sulphide deposits in South
759 China: *Ore Geology Reviews*, v. 31, no. 1, p. 107-138.
- 760 Heinrich, C. A., and Seward, T. M., 1990, A spectrophotometric study of aqueous iron
761 (II) chloride complexing from 25 to 200°C: *Geochimica et Cosmochimica*
762 *Acta*, v. 54, no. 8, p. 2207-2221.
- 763 Hinman, M., 1996, Constraints, timing and processes of stratiform base metal
764 mineralisation at the HYC Ag-Pb-Zn deposit, McArthur River, New
765 developments in metallogenic research: *The McArthur, Mount Isa, Cloncurry*
766 *Minerals Province, Volume 56: Townsville, EGRU*, p. 56-59.
- 767 Ireland, T., Large, R. R., McGoldrick, P., and Blake, M., 2004, Spatial distribution
768 patterns of sulfur isotopes, nodular carbonate, and ore textures in the
769 McArthur River (HYC) Zn-Pb-Ag deposit, Northern Territory, Australia:
770 *Economic Geology*, v. 99, no. 8, p. 1687-1709.
- 771 Kampschulte, A., and Strauss, H., 2004, The sulfur isotopic evolution of Phanerozoic
772 seawater based on the analysis of structurally substituted sulfate in carbonates:
773 *Chemical Geology*, v. 204, no. 3, p. 255-286.
- 774 Kozdon, R., Kita, N. T., Huberty, J. M., Fournelle, J. H., Johnson, C. A., and Valley, J.
775 W., 2010, In situ sulfur isotope analysis of sulfide minerals by SIMS:
776 Precision and accuracy, with application to thermometry of ~3.5 Ga Pilbara
777 cherts: *Chemical Geology*, v. 275, no. 3, p. 243-253.
- 778 Lai, Y., 1996, Devoian-Carboniferous sedimentary basin structure and stratatound
779 deposits in Guangdong: *Guangdong Geology*, v. 11, no. 2, p. 27-37. (in
780 Chinese with English abstract).
- 781 Large, R. R., Bull, S. W., Cooke, D. R., and McGoldrick, P. J., 1998, A genetic model
782 for the H.Y.C. Deposit, Australia: Based on regional sedimentology,

- 783 geochemistry, and sulfide-sediment relationships: *Economic Geology*, v. 93,
784 no. 8, p. 1345-1368.
- 785 Large, R. R., Bull, S. W., McGoldrick, P. J., and Walters, S., 2005, Stratiform and
786 strata-bound Zn-Pb-Ag deposits in Proterozoic sedimentary basins, northern
787 Australia: *Economic Geology*, v. 100, p. 931-963.
- 788 Large, R. R., Bull, S. W., Selley, D., Yang, J., Cooke, D., Garven, G., and
789 McGoldrick, P., 2002, Controls on the formation of giant stratiform sediment-
790 hosted Zn-Pb-Ag deposits: With particular reference to the north Australian
791 Proterozoic: University of Tasmania, Centre for Ore Deposit Research Special
792 Publication, v. 4, p. 107-149.
- 793 Leach, D., Sangster, D., Kelley, K., Large, R. R., Garven, G., Allen, C., Gutzmer, J.,
794 and Walters, S., 2005, Sediment-hosted lead-zinc deposits: A global
795 perspective: *Economic Geology*, v. 100, p. 561-607.
- 796 Leach, D. L., Marsh, E., Emsbo, P., Rombach, C. S., Kelley, K. D., and Anthony, M.,
797 2004, Nature of Hydrothermal Fluids at the Shale-Hosted Red Dog Zn-Pb-Ag
798 Deposits, Brooks Range, Alaska: *Economic Geology*, v. 99, no. 7, p. 1449-
799 1480.
- 800 Lin, Z., Sun, X., Strauss, H., Lu, Y., Gong, J., Xu, L., Lu, H., Teichert, B. M. A., and
801 Peckmann, J., 2017, Multiple sulfur isotope constraints on sulfate-driven
802 anaerobic oxidation of methane: Evidence from authigenic pyrite in seepage
803 areas of the South China Sea: *Geochimica et Cosmochimica Acta*, v. 211, p.
804 153-173.
- 805 Lyons, T. W., 1997, Sulfur isotopic trends and pathways of iron sulfide formation in
806 upper Holocene sediments of the anoxic Black Sea: *Geochimica et*
807 *Cosmochimica Acta*, v. 61, no. 16, p. 3367-3382.
- 808 Lyons, T. W., Gellatly, A. M., McGoldrick, P. J., and Kah, L. C., 2006, Proterozoic
809 sedimentary exhalative (SEDEX) deposits and links to evolving global ocean
810 chemistry: *Geological Society of America Memoirs*, v. 198, p. 169-184.
- 811 Machel, H. G., 2001, Bacterial and thermochemical sulfate reduction in diagenetic
812 settings-old and new insights: *Sedimentary Geology*, v. 140, no. 1-2, p. 143-
813 175.
- 814 Magnall, J. M., Gleeson, S. A., and Paradis, S., 2015, The importance of siliceous
815 radiolarian-bearing mudstones in the formation of sediment-hosted Zn-Pb±Ba
816 mineralization in the Selwyn Basin, Yukon, Canada: *Economic Geology*, v.
817 110, no. 8, p. 2139-2146.
- 818 Magnall, J. M., Gleeson, S. A., Stern, R. A., Newton, R. J., Poulton, S. W., and
819 Paradis, S., 2016, Open system sulphate reduction in a diagenetic environment
820 – Isotopic analysis of barite ($\delta^{34}\text{S}$ and $\delta^{18}\text{O}$) and pyrite ($\delta^{34}\text{S}$) from the Tom

821 and Jason Late Devonian Zn–Pb–Ba deposits, Selwyn Basin, Canada:
 822 *Geochimica et Cosmochimica Acta*, v. 180, p. 146-163.

823 Mason, P. R., Košler, J., de Hoog, J. C., Sylvester, P. J., and Meffan-Main, S., 2006, In
 824 situ determination of sulfur isotopes in sulfur-rich materials by laser ablation
 825 multiple-collector inductively coupled plasma mass spectrometry (LA-MC-
 826 ICP-MS): *Journal of Analytical Atomic Spectrometry*, v. 21, no. 2, p. 177-186.

827 Metcalfe, I., 2006, Palaeozoic and Mesozoic tectonic evolution and palaeogeography
 828 of East Asian crustal fragments: The Korean Peninsula in context: *Gondwana*
 829 *Research*, v. 9, no. 1, p. 24-46.

830 Neretin, L. N., Böttcher, M. E., and Grinenko, V. A., 2003, Sulfur isotope
 831 geochemistry of the Black Sea water column: *Chemical Geology*, v. 200, no. 1,
 832 p. 59-69.

833 Pan, J., and Zhang, Q., 1994, A preliminary discussion on geochemical characteristics
 834 and genesis of the Dajiangping pyrite deposit, western Guangdong Province:
 835 *Mineral deposits*, v. 13, no. 3, p. 231-241. (in Chinese with English abstract).

836 Pei, T., 1989, Geological Characteristics and Genesis of the Hongyan pyrite deposits
 837 in Yinde County, Guangdong Province: *Mineral Deposits*, v. 8, no. 2, p. 81-90.
 838 (in Chinese with English abstract).

839 Perkins, W. G., and Bell, T. H., 1998, Stratiform replacement lead-zinc deposits: A
 840 comparison between Mount Isa, Hilton, and McArthur River: *Economic*
 841 *Geology*, v. 93, no. 8, p. 1190-1212.

842 Qiu, W. J., Zhou, M.-F., and Liu, Z. R., 2018, Late Paleozoic SEDEX deposits in
 843 South China formed in a carbonate platform at the northern margin of
 844 Gondwana: *Journal of Asian Earth Sciences*, v. 156, p. 41-58.

845 Rajabi, A., Rastad, E., Canet, C., and Alfonso, P., 2014, The early Cambrian Chahmir
 846 shale-hosted Zn–Pb deposit, Central Iran: an example of vent-proximal
 847 SEDEX mineralization: *Mineralium Deposita*, v. 50, no. 5, p. 1-20.

848 Sangster, D. F., 2002, The role of dense brines in the formation of vent-distal
 849 sedimentary-exhalative (SEDEX) lead–zinc deposits: field and laboratory
 850 evidence: *Mineralium Deposita*, v. 37, no. 2, p. 149-157.

851 Sangster, D. F., 2017, Toward an integrated genetic model for vent-distal SEDEX
 852 deposits: *Mineralium Deposita*, p. 1-19.

853 Seal, R. R., 2006, Sulfur isotope geochemistry of sulfide minerals: Reviews in
 854 *Mineralogy and Geochemistry*, v. 61, no. 1, p. 633-677.

855 Sim, M. S., Bosak, T., and Ono, S., 2011, Large sulfur isotope fractionation does not
 856 require disproportionation: *Science*, v. 333, no. 6038, p. 74-77.

857 Stacey, J. S., and Kramers, J. D., 1975, Approximation of terrestrial lead isotope
 858 evolution by a two-stage model: *Earth and Planetary Science Letters*, v. 26, no.

- 2, p. 207-221.
- Turner, J. S., and Campbell, I. H., 1987, Temperature, density and buoyancy fluxes in “black smoker” plumes, and the criterion for buoyancy reversal: *Earth and Planetary Science Letters*, v. 86, no. 1, p. 85-92.
- Ulrich, T., Long, D., Kamber, B., and Whitehouse, M., 2011, In situ trace element and sulfur isotope analysis of pyrite in a paleoproterozoic gold placer deposit, Pardo and Clement Townships, Ontario, Canada: *Economic Geology*, v. 106, no. 4, p. 667-686.
- Wan, Y., Liu, D., Wilde, S. A., Cao, J., Chen, B., Dong, C., Song, B., and Du, L., 2010, Evolution of the Yunkai Terrane, South China: Evidence from SHRIMP zircon U–Pb dating, geochemistry and Nd isotope: *Journal of Asian Earth Sciences*, v. 37, no. 2, p. 140-153.
- Wang, D., Zheng, J., Ma, Q., Griffin, W. L., Zhao, H., and Wong, J., 2013a, Early Paleozoic crustal anatexis in the intraplate Wuyi-Yunkai orogen, South China: *Lithos*, v. 175, p. 124-145.
- Wang, H., Li, H., Wang, Y., and Wang, H., 1996, The mineralization age of Guangdong Dajiangping massive sulfide deposit- Rb-Sr isotopic study of siliceous rock: *Chinese Science Bulletin*, v. 41, no. 21, p. 1960-1962. (in Chinese with English abstract).
- Wang, Y., Zhang, A., Fan, W., Zhang, Y., and Zhang, Y., 2013b, Origin of paleosubduction-modified mantle for Silurian gabbro in the Cathaysia Block: Geochronological and geochemical evidence: *Lithos*, v. 160–161, no. 0, p. 37-54.
- Wang, Y., Zhang, Y., Fan, W., and Peng, T., 2005, Structural signatures and $^{40}\text{Ar}/^{39}\text{Ar}$ geochronology of the Indosinian Xuefengshan tectonic belt, South China Block: *Journal of Structural Geology*, v. 27, no. 6, p. 985-998.
- Williams, N., 1978, Studies of the base metal sulfide deposits at McArthur River, Northern Territory, Australia; I, The Cooley and Ridge deposits: *Economic Geology*, v. 73, no. 6, p. 1005-1035.
- Wing, B. A., and Halevy, I., 2014, Intracellular metabolite levels shape sulfur isotope fractionation during microbial sulfate respiration: *Proceedings of the National Academy of Sciences*, v. 111, no. 51, p. 18116-18125.
- Xu, K., Wang, H., Zhou, J., and Zhu, J., 1996, A discussion on the exhalative sedimentary massive sulfide deposits of South China: *Geological Journal of China Universities*, v. 3, p. 242-257. (in Chinese with English abstract).
- Yang, Z., Chen, K., Cheng, S., Mao, X., and Jiang, D., 1996, Late Paleozoic sedimentary basin-extension and metallogenic in the northern Guangdong Province, China: *Geology and Mineral Resources of South China*, v. 3, p. 23-

- 897 30. (in Chinese with English abstract).
- 898 Zhang, B., Zhang, Q., and Pan, J., 1994, Trace element characteristics and their
 899 geological significance of Dajiangping Pyrite Deposit, Western Guangdong:
 900 Geology and Prospecting, v. 30, no. 4, p. 66-71. (in Chinese with English
 901 abstract).
- 902 Zhang, Q., Zhang, B., Cao, Y., Pan, J., Zeng, t., and Hao, s., 1993, Priliminary
 903 discussion on sulfur and lead isotope compositions of the Dajiangping Pyrite
 904 Deposit in Western Guangdong Province: Acta Geologica Sinica, v. 67, no. 3,
 905 p. 232-243. (in Chinese with English abstract).
- 906 Zhang, Q., Zhang, B., Pan, J., and Cao, Y., 1992, The characteristics and REE element
 907 pattern of hydrothermal sedimentary siliceous rock in Dajiangping Pyrite
 908 Deposit: Chinese Science Bulletin, v. 37, no. 17, p. 1588-1591. (in Chinese
 909 with English abstract).
- 910 Zhang, X., Xu, X., Xia, Y., and Liu, L., 2017, Early Paleozoic intracontinental
 911 orogeny and post-orogenic extension in the South China Block: Insights from
 912 volcanic rocks: Journal of Asian Earth Sciences, v. 141, p. 24-42.
- 913 Zhao, J., Zhou, M.-F., Yan, D., Zheng, J., and Li, J., 2011, Reappraisal of the ages of
 914 Neoproterozoic strata in South China: no connection with the Grenvillian
 915 orogeny: Geology, v. 39, no. 4, p. 299-302.
- 916 Zhao, X., Mark B, A., Andrew G, W., and Simon P, P., 1996, Rift-related Devonian
 917 sedimentation and basin development in South China: Journal of Southeast
 918 Asian Earth Sciences, v. 14, no. 1, p. 37-52.
- 919 Zhong, Z., You, Z., Zhou, H., and Han, Y., 1996, The evolution and basic structural
 920 framework of the basement of the Yunkai uplift: Regional Geology of China,
 921 v. 1, p. 36-43. (in Chinese with English abstract).
- 922 Zhou, Y., 1990, On sedimentary geochemistry of siliceous rocks originated from
 923 hydrothermal water in the Nandan-Hechi Basin: Acta Sedimentologica Sinica,
 924 v. 8, no. 3, p. 75-83. (in Chinese with English abstract).

925

926

927

928

929

930 **Figure captions**

931 Fig. 1. A map of southern China showing the location of the Dajiangping pyrite deposit,
932 SEDEX Pb-Zn deposits, SEDEX barite deposits, major structural elements and the
933 distribution of Devonian-Carboniferous sedimentary strata.

934

935 Fig. 2. A simplified geological map of the Yunfu region. Modified from the Yunfu
936 Dagangshan 1:50000 geological map of the region ([BGE723BGD, 1965](#)).

937

938 Fig. 3. A geological map of the Dajiangping deposit. The locations of cross-section A-
939 B and cross-section C-D are identified on the map. Modified from a local geological
940 map of the Dajiangping deposit ([BGE723BGD, 1965](#)).

941

942 Fig. 4. Photographs of the stratiform orebodies and different types of pyrite ores from
943 open pit of the Dajiangping pyrite deposit. A and B. Stratiform pyrite orebodies showing
944 the conformable nature of the mineralization; C. Laminated pyrite ore intercalated with
945 black shale; D. A 'Slump fold' developed in laminated pyrite ore; E. Massive pyrite ore
946 with a weakly preserved laminar structure and minor sedimentary clasts; F. Laminated
947 pyrite ore intercalated with black shale, chert and siltstone; G. Massive pyrite ore cut
948 by quartz veins; H. Laminated pyrite ore crosscut by deformed massive pyrite ore.

949

950 Fig. 5. Schematic stratigraphic columns and images of representative drill hole samples
951 from each sedimentary and mineralized unit. The stratigraphy was established from drill
952 hole YF02, which penetrates the stratigraphic interval hosting the deposit adjacent to
953 mineralization, and is subdivided into three sedimentary units, namely the Lower Unit,
954 Middle Unit and Upper Unit. The mineralized stratigraphy of the orebodies was
955 established from drill hole YF04, which penetrates the full mineralized succession in
956 the center of deposit, and is subdivided into four mineralized units, namely M1, M2,
957 M3 and M4.

958

959 Fig. 6. Photomicrographs of carbonaceous limestone from the strata hosting the ore and
960 mica-quartz schist from the metamorphic basement below the deposit. A and B. Typical
961 carbonaceous limestone containing crinoid and brachiopod fossils; C and D. Mica-
962 quartz schist.

963

964 Fig. 7. Photomicrographs of typical laminated pyrite ore and black shale taken in
965 reflected and transmitted light. A. A hand specimen of laminated pyrite ore consisting
966 of pyrite layers, black shale layers and siltstone layers. B and D. Enlargements of parts
967 of pyrite layers composed of coarse-grained pyrite (B1, D1), quartz and calcite. The

968 quartz and calcite occur between the pyrite crystals and display a comb-texture
 969 perpendicular to the crystal faces of pyrite grains (B2, D2). C. Black shale layers
 970 composed of bedding-parallel muscovite/illite and quartz (C2) with minor disseminated
 971 fine-grained pyrite (C1). E. Siltstone layers dominated by quartz and clasts of other
 972 silicate minerals and muscovite/illite (E2) with minor disseminated fine-grained pyrite
 973 (E1). Py=Pyrite, Qz=quartz, Cal=calcite, Ms=Muscovite.

974

975 Fig. 8. Photomicrographs showing representative textures of the laminated pyrite ores
 976 under reflected light. A. Laminated pyrite ores showing the intercalation of detrital
 977 sedimentary layers with fine-grained pyrite (*Pyrite 1*) and pyrite layers composed of
 978 coarse-grained pyrite aggregates (*Pyrite 2*). B. A gradual transition from thick coarse-
 979 grained pyrite layers (*Pyrite 2*) to layers of fine-grained pyrite (*Pyrite 1*). C. Cubes and
 980 needles of *Pyrite 1* and coarse anhedral-subhedral *Pyrite 2*; D. Small euhedra of *Pyrite*
 981 *1* enclosed in a large subhedral *Pyrite 2* crystal. E and F. Overgrowths of anhedral *Pyrite*
 982 *2* on fine-grained *Pyrite 1* aggregates. Py1=*Pyrite 1*, Py 2=*Pyrite 2*, Qz=quartz,
 983 Cal=calcite, Kfs=K-feldspar.

984

985 Fig. 9. A and B. Photographs of thin sections showing *Pyrite 3* in fractures (diagenetic?)
 986 and pore spaces between sedimentary layers. C. Reflected light image of anhedral

987 *Pyrite 3* and pyrrhotite (Po) in the interstices between sedimentary clasts. D. Porous
 988 *Pyrite 3* (Py3) and pyrrhotite (Po). E. *Pyrite 3* (Py3) filling pores between clasts. F.
 989 Pyrrhotite in a fracture (diagenetic?) cutting black shale. Py 3=*Pyrite 3*, Po=pyrrhotite.
 990

991 Fig. 10. Stratigraphic profiles showing concentrations of S, C_{org} (Organic carbon),
 992 TFe₂O₃ (total iron), Al₂O₃, SiO₂, MnO and ZnO+PbO against depth in drill hole YF04
 993 (Table 1). Also shown is the stratigraphic column for drill hole YF04 illustrating the
 994 distribution of the various ore and sedimentary units. The filled black spots represent
 995 samples of laminated ores, the hollow circles represent samples of black shale or low
 996 grade ores.

997
 998 Fig. 11. Binary plots of the concentrations of S vs. Fe, Al₂O₃ vs. Fe₂O₃, Al₂O₃ vs. TiO₂,
 999 Al₂O₃ vs. K₂O, SiO₂/Al₂O₃ vs. K₂O/Al₂O₃, SiO₂/Al₂O₃ vs. TiO₂, S vs. C_{org} and S vs.
 1000 C_{org}/Al for bulk samples from drill hole YFO2 and YF04. The filled black spots
 1001 represent samples of laminated ores from drill hole YF04, the hollow circles represent
 1002 samples of black shale from drill hole YF04 and the grey squares represent samples of
 1003 black shale from the Upper Unit in drill hole YF02.

1004
 1005 Fig. 12. Histograms showing net mass changes of elements and oxides for ores from

1006 the three major mineralized units (M2, M3, M4) of drill hole YF04 relative to the
1007 unmineralized black shale in the Upper Unit intersected in drill hole YF02 ~1km south
1008 of the deposit.

1009

1010 Fig. 13. Lead isotope compositions of *Pyrite 1* and 2 in the laminated ores. Also shown
1011 is the Pb isotope composition (asterisks and shaded area) of the metamorphic basement
1012 rocks in the Wuchuan-Sihui region (Zhang et al., 1993). The growth curves of two stage
1013 evolution model of Stacey and Kramer (Stacey and Kramers, 1975) with $\mu=9.5$ and
1014 $\mu=11$ are shown in $^{206}\text{Pb}/^{204}\text{Pb}$ vs $^{207}\text{Pb}/^{204}\text{Pb}$.

1015

1016 Fig. 14. Images of the laminated pyrite ores in three representative samples from drill
1017 hole YF04 showing the in-situ-determined $\delta^{34}\text{S}$ values of *Pyrite 1* and 2 crystals. A to
1018 C. The $\delta^{34}\text{S}$ values of *Pyrite 1* and 2 crystals are all negative and very similar in a single
1019 sample, either within single layers or in multiple layers. Py1=*Pyrite 1*, Py 2=*Pyrite 2*.

1020

1021 Fig. 15. Variation of $\delta^{34}\text{S}$ values of each analyze spots of *Pyrite 1* and *Pyrite 2* of
1022 different laminations in two representative laminated ore samples YF10-2 and YF46-1.

1023

1024 Fig. 16. A to E. Images showing *Pyrite 3* and pyrrhotite crystals in five representative

1025 black shale samples. The pyrite crystals all have positive $\delta^{34}\text{S}$ values, some of which
1026 vary considerably in the same sample. Py 3=*Pyrite 3*, Po=pyrrhotite.

1027

1028 Fig. 17. A histogram of sulfur isotopic compositions for the different pyrite types
1029 representing results of both in-situ analyses and analyses of pyrite separates. The
1030 samples were taken from both drill holes and the open pit. *Pyrite 1 and 2* crystals and
1031 pyrite separates of laminated pyrite ores exhibit a wide range of $\delta^{34}\text{S}$ values, although
1032 most of them are concentrated between -16 ‰ and -30 ‰. *Pyrite 3* crystals mostly have
1033 positive $\delta^{34}\text{S}$ values with a mode of ~5 ‰. Py1=*Pyrite 1*, Py 2=*Pyrite 2*, Py 3=*Pyrite 3*.

1034

1035 Fig. 18 A cartoon showing a model for the formation of the Dajiangping pyrite deposit.

1036 A. Syn-sedimentary sulfide deposition is associated with the venting of hydrothermal
1037 fluids and their mixing with seawater in a H_2S -rich basin that experienced intense
1038 sulfate-reducing bacterial activity, producing pyrite with strongly negative $\delta^{34}\text{S}$ values.

1039 B. Rapid crystallization of *Pyrite 1* in a mushrooming column, in which vent fluid
1040 mixed with H_2S -rich seawater, and slower crystallization of *Pyrite 2* as the column
1041 collapses and the fluid collects on the seafloor and infiltrates the underlying sediment.

1042 C. Percolation of fresh seawater into fractures and pores of muds during diagenesis,
1043 leading to the crystallization of *Pyrite 3* and pyrrhotite by thermochemical sulfate

1044 reduction (TSR) and anaerobic oxidation of methane coupled to sulfate reduction

1045 (AOM-SR). Py1=*Pyrite 1*, Py 2=*Pyrite 2*, Py 3=*Pyrite 3*, Po =pyrrhotite.

1046

1047

1048

1049

1050

1051

1052

1053

1054

1055

1056

1057

1058

1059

1060

1061

1062 **Appendix**

1063 ***Analysis of major element and organic carbon concentrations in bulk samples***

1064 Major element and organic carbon concentrations of the bulk samples were analyzed
1065 by ALS Minerals/ALS Chemex Co. Ltd, Guangzhou, China.

1066 ***Pyrite ores with high sulfur contents (>3 wt.%):***

1067 A powdered sample (0.2 g) was added to a lithium metaborate/lithium tetraborate flux
1068 (0.9 g), mixed well and fused in a furnace at 1000°C. The resulting melt was then cooled
1069 and dissolved in 100 mL of 4% nitric acid/2% hydrochloric acid. This solution was
1070 analyzed by ICP-AES and the results were corrected for spectral inter-element
1071 interferences. The oxide concentration was calculated from the elemental concentration
1072 and the result was reported in that format.

1073 ***Sedimentary rocks with low sulfur contents (<3 wt.%):***

1074 A calcined or ignited sample (0.9 g) was added to 9 g of lithium borate flux (50% - 50%
1075 $\text{Li}_2\text{B}_4\text{O}_7$ – LiBO_2), mixed well and fused in an auto fluxer between 1050 - 1100°C. A
1076 flat molten glass disc was prepared from the resulting melt. This disc was then analysed
1077 by X-ray fluorescence spectrometry. The organic carbon content was measured using a
1078 LECO CS-200 analyzer after the samples had been treated with hydrochloric acid to
1079 remove carbonates.

1080 ***In-situ sulfur isotope analyses by LA-MC-ICPMS***

1081 In-situ sulfur isotope analyses of the pyrite were performed using a Nu Plasma 1700

1082 MC-ICP-MS (Nu instruments, UK) equipped with a Resolution M-50 193nm ArF
1083 Excimer laser ablation system at the State Key Laboratory of Continental Dynamics,
1084 Northwest University, Xi'an, China (Bao et al., 2017; Chen et al., 2017). Samples were
1085 ablated in He gas (gas flow = 0.28 L/min) and Ar gas (gas flow = 0.96 L/min) within a
1086 two-volume chamber (Laurin Technic S-155). Sulfur isotope concentrations were
1087 analyzed at high resolution. During the ablation, data were collected in a static mode
1088 (^{32}S , ^{34}S). Single spots of pyrite grains were ablated at a spatial resolution of 37 to 53
1089 μm , using a fluence of 3.7 J/cm² at 2-4 Hz. The total S signal obtained for pyrite was
1090 typically 8-12 V. Under these conditions, after a 30 s baseline, 50 s of ablation was
1091 needed to obtain an internal precision of $^{34}\text{S}/^{32}\text{S} \leq \pm 0.000002$ (1 SE). Two pyrite
1092 standards were used for external standard bracketing (Py-4) and quality control (PTST-
1093 2) of analyses (Chen et al., 2017). Their $\delta^{34}\text{S}_{\text{CDT}}$ values had been determined by GS-
1094 MS or solution introduced MC-ICP-MS. For a $\delta^{34}\text{S}_{\text{CDT}}$ (‰) value of 32.5 ‰ of PTST-
1095 2, the average value was determined to be 33 ± 0.6 (2SD, n=63). The external precision
1096 of the standard is less than 0.3 (2SD, n=150).

1097 Additional in-situ S isotope analyses of pyrite were performed at the laboratory of
1098 the Geological Survey of Finland in Espoo using a Nu Plasma HR multicollector
1099 ICPMS equipped with a Photon Machine Analyte G2 laser microprobe (Müller et al.,
1100 2009). Samples were ablated at a spatial resolution of 50 μm , using a fluence of 0.83

1101 J/cm² at 5Hz. The total S signal obtained for pyrite was typically 1.9-2.3 V. Under these
1102 conditions, after a 20 s baseline, 50-60 s of ablation was needed to obtain an internal
1103 precision of $^{34}\text{S}/^{32}\text{S} \leq \pm 0.000005$ (1 SE). Two pyrite standards were used for
1104 external standard bracketing (PPP-1) and quality control (Py2) of analyses (Gilbert et
1105 al., 2014). The in-house standard Py2 was previously measured by gas mass
1106 spectrometry. For a $\delta^{34}\text{S}_{\text{CDT}}$ (‰) value of -0.4 ± 0.5 ‰ (1s), the average value was -
1107 0.22 ± 0.35 (1s, n=35).

1108 *Sulfur isotope composition of pyrite separates*

1109 Sulfur isotope analyses of the pyrite separates were carried out at the State Key
1110 Laboratory of Environmental Geochemistry, Institute of Geochemistry (Guiyang),
1111 Chinese Academy of Sciences. Mineral separates were extracted from crushed and
1112 washed sample fragments and were selected by handpicking under a binocular
1113 microscope to achieve a purity of >99%. Sulfur was extracted with a continuous flow
1114 device, wherein 0.2 to 0.3 mg of sulfide was converted to SO₂ in an EA-IsoPrime
1115 isotope ratio mass spectrometer (Euro3000, GV instruments). The $\delta^{34}\text{S}$ values are
1116 reported relative to the Canyon Diablo Troilite standard (CDT) and were calibrated by
1117 the international standard sample GBW-4414 (Ag₂S, $\delta^{34}\text{S} = -0.07$ ‰).

1118 *In-situ lead isotope analyses by LA-MC-ICPMS*

1119 In-situ lead isotopic analyses of pyrite and chalcopyrite were conducted on 50 - 100-

1120 μm -thick polished sections, using a Nu PlasmaTM multi-collector ICPMS with a
 1121 femtosecond laser ablation system (NWR UPFemto, ESI, USA) (fLA-MC-ICPMS) at
 1122 the State Key Laboratory of Continental Dynamics, Northwest University, Xian, China.
 1123 A detailed description of the analytical procedure is available in Chen et al. (2014) and
 1124 Yuan et al. (2013). Argon and helium were used as the carrier gases for laser ablation.
 1125 The aerosol from the ablation cell was mixed with Tl (argon with Tl) in a glass aerosol
 1126 homogenizer and then introduced into the ICP for atomization and ionization. During
 1127 the instrumental analysis, the intensities of the ion beams of ^{202}Hg , ^{203}Tl , $^{204}\text{Pb} + \text{Hg}$,
 1128 ^{205}Tl , ^{206}Pb , ^{207}Pb and ^{208}Pb were monitored simultaneously with Faraday collectors L4,
 1129 L3, L2, L1, Ax, H1 and H2, respectively. The concentrations of lead and mercury in the
 1130 gas blank were lower than 10 and 20 pg/l, respectively, and thus their contributions to
 1131 the analyses were negligible. Thallium was used to monitor and correct for instrumental
 1132 mass discrimination, and ^{202}Hg was used to correct for the isobaric overlap of ^{204}Hg on
 1133 ^{204}Pb . The interference of ^{204}Hg on ^{204}Pb was corrected to enable use of the natural
 1134 abundance ratio $^{204}\text{Hg}/^{202}\text{Hg} = 0.229883$ ($^{202}\text{Hg} = 0.29863$ and $^{204}\text{Hg} = 0.06865$)
 1135 adjusted for instrumental mass fractionation as monitored by the $^{205}\text{Tl}/^{203}\text{Tl}$ ratio. The
 1136 $^{204}\text{Hg}/^{204}\text{Pb}$ ratios varied from day to day, but they were <20 ppm in the experimental
 1137 system when the ion beam of ^{204}Pb had an intensity >0.25 V.
 1138 The acquisition of the MC-ICP-MS data employed the time-resolved analysis

1139 (TRA) mode with an integration time of 0.2 s, and laser ablation was performed in the
 1140 line scan ablation mode at a speed of 5 $\mu\text{m/s}$ with the laser beam focused on the sample
 1141 surface. Each line scan analysis consisted of background collection for 40 s followed
 1142 by an additional 50 s of ablation for signal collection and 40 s of wash time to reduce
 1143 memory effects and to allow the instrument to stabilize after each analysis. All of the
 1144 recorded Pb and Hg signals were corrected for background by subtracting the
 1145 background signals (gas blank and dark noise signals) from the corresponding gross
 1146 signals (signals obtained after firing the laser), whereas the Tl signals were corrected
 1147 for background by subtracting the average dark noise signals (stability 25 ppm at 10
 1148 min). To ensure the stability of the ^{208}Pb signal obtained from different samples with
 1149 disparate Pb concentrations, samples were ablated with laser line scans approximately
 1150 120 μm in length and 30–65 μm in width with adjustable laser frequency. NIST SRM
 1151 610 was used as a quality control sample (Yuan et al. 2013), and was analyzed once for
 1152 every five sample points. The average Pb isotopic compositions of NIST SRM 610 in
 1153 this study are: $^{208}\text{Pb}/^{204}\text{Pb} = 36.981 \pm 0.004$; $^{207}\text{Pb}/^{204}\text{Pb} = 15.515 \pm 0.001$; $^{206}\text{Pb}/^{204}\text{Pb}$
 1154 $= 17.052 \pm 0.001$ (1σ), and are similar to those of the reference values of NIST SRM610:
 1155 $^{208}\text{Pb}/^{204}\text{Pb}=36.964 \pm 0.022$; $^{207}\text{Pb}/^{204}\text{Pb}=15.504 \pm 0.001$; $^{206}\text{Pb}/^{204}\text{Pb} = 17.045 \pm 0.008$
 1156 (2σ).

Table 1

Major element compositions of bulk samples of pyrite ores and sedimentary rocks from drill hole YF04 and black shale from drill hole YF02.

Sample	YF04-01	YF04-02	YF04-03	YF04-04	YF04-05	YF04-06	YF04-07	YF04-08	YF04-09	YF04-10	YF04-11	YF04-12	YF04-13	YF04-14	YF04-15	YF04-16	YF04-17	YF04-18
Rock	Ore	Host	Host	Ore	Ore	Ore	Ore	Ore	Host	Host	Host	Host	Host	Host	Ore	Host	Host	Host
Depth(m)	35.4	36.0	37.6	38.2	41.0	43.5	45.0	47.0	50.0	54.0	56.0	59.0	62.5	68.0	70.0	77.0	81.0	85.0
S(%)	2.98	2.59	26.84	18.84	18.52	21.00	22.48	1.45	1.75	1.75	1.65	1.77	1.93	6.18	1.46	1.00	1.62	26.52
Corg(%)	0.87	1.57	1.58	0.88	0.66	0.80	0.76	0.70	1.71	2.21	1.19	1.26	1.47	2.20	1.34	1.40	0.95	1.41
Major oxides (wt. %)																		
SiO ₂	36.23	56.88	61.95	39.33	28.73	38.96	42.54	39.74	68.66	69.96	69.19	65.15	64.10	75.46	61.45	71.71	67.14	68.47
Al ₂ O ₃	5.63	12.48	11.66	3.66	5.31	7.54	6.95	6.10	13.38	11.22	13.20	10.83	12.07	5.02	12.35	10.14	14.25	14.60
Fe ₂ O _{3t}	33.26	4.00	3.40	33.70	23.67	22.17	26.68	28.59	3.66	4.18	3.68	3.39	4.24	4.91	11.24	3.45	3.83	4.04
K ₂ O	1.54	3.28	3.16	1.05	1.49	2.18	2.16	1.94	3.76	3.64	4.15	3.29	3.53	1.48	3.60	2.90	4.39	4.71
Na ₂ O	0.04	0.06	0.04	0.03	0.04	0.05	0.04	0.04	0.12	0.05	0.10	0.04	0.10	0.01	0.11	0.10	0.10	0.08
CaO	1.38	6.87	6.05	1.25	13.15	5.96	2.56	2.82	1.88	1.90	2.07	6.33	5.97	4.72	1.66	3.65	2.77	0.97
MgO	0.67	2.02	1.70	0.56	1.08	0.93	0.74	0.73	1.68	1.34	1.00	0.88	1.33	0.63	1.96	1.09	1.46	1.32
MnO	0.24	0.84	0.73	0.16	1.38	0.80	0.33	0.33	0.10	0.11	0.08	0.18	0.15	0.15	0.11	0.17	0.10	0.06
BaO	0.55	0.97	0.82	0.24	0.34	0.53	0.37	0.26	0.18	0.12	0.16	0.15	0.17	0.05	0.16	0.09	0.09	0.13
P ₂ O ₅	0.05	0.06	0.07	0.04	0.07	0.06	0.05	0.05	0.07	0.05	0.07	0.05	0.06	0.06	0.12	0.08	0.06	0.06
TiO ₂	0.29	0.51	0.46	0.17	0.29	0.31	0.29	0.30	0.48	0.39	0.60	0.42	0.46	0.18	0.58	0.45	0.60	0.55
PbO	0.05	ND	ND	0.06	0.06	0.05	0.04	0.05	ND	ND	ND	ND	ND	ND	0.04	ND	ND	ND
ZnO	0.02	ND	ND	0.02	0.03	2.51	0.20	0.11	ND	ND	ND	ND	ND	ND	0.24	ND	ND	ND
Total	79.95	87.97	90.04	80.27	75.64	82.05	82.95	81.06	93.97	92.96	94.30	90.71	92.18	92.67	93.62	93.83	94.79	94.99

Notes: Host = host sedimentary rock; Ore = laminated pyrite ore; ND = not detected; low totals are due to losses of sulfur, H₂O, and/or CO₂.

Sample	YF04-19	YF04-20	YF04-22	YF04-23	YF04-24	YF04-25	YF04-26	YF04-27	YF04-28	YF04-29	YF04-30	YF04-31	YF04-32	YF04-33	YF04-33B	YF04-34	YF04-35	YF04-36
Rock	Ore	Host	Host	Host	Ore	Ore	Ore	Ore	Ore	Ore	Ore	Ore	Ore	Ore	Ore	Ore	Ore	Ore
Depth(m)	90.5	91.5	98.0	100.0	109.0	113.0	115.0	117.0	121.0	124.0	133.0	136.0	141.0	145.0	149.0	155.0	157.0	164.0
S(%)	4.50	2.86	2.26	2.99	14.12	29.28	7.58	26.12	11.48	18.32	21.96	19.88	23.96	8.60	5.78	10.04	20.24	6.38
C org(%)	0.71	0.96	1.43	0.78	1.09	1.22	0.30	0.65	0.68	0.71	1.03	0.93	0.47	0.64	0.48	0.84	0.69	1.21
Major oxides (wt. %)																		
SiO ₂	63.65	64.78	38.61	65.21	52.24	35.56	68.62	36.46	59.93	41.04	36.76	42.34	36.96	57.05	65.13	41.94	40.26	39.23
Al ₂ O ₃	14.45	16.29	8.56	13.40	10.50	3.14	8.04	6.78	9.84	10.10	10.25	10.00	8.12	6.96	11.00	6.26	8.48	6.92
Fe ₂ O _{3t}	7.11	4.82	3.98	5.07	17.83	36.46	9.46	32.56	14.88	23.17	28.27	25.67	29.76	10.78	7.63	12.64	25.67	7.83
K ₂ O	4.13	4.87	0.82	3.99	2.61	0.48	2.49	1.40	2.80	3.00	3.13	2.93	1.66	1.80	2.88	1.31	2.03	2.40
Na ₂ O	0.16	0.17	0.24	0.13	0.15	0.09	0.05	0.13	0.13	0.09	0.11	0.11	0.09	0.08	0.08	0.09	0.13	0.08
CaO	1.87	1.64	24.7	3.73	2.75	2.11	1.72	1.81	1.69	4.80	3.19	1.71	3.67	9.20	4.08	16.65	5.01	18.65
MgO	1.48	1.38	1.04	1.40	0.81	0.29	0.60	0.80	0.92	1.00	0.66	0.84	0.99	0.84	1.50	0.85	0.92	1.23
MnO	0.11	0.09	0.76	0.18	0.34	0.16	0.30	0.47	0.22	0.40	0.14	0.27	0.91	0.90	0.72	0.91	1.19	1.19
BaO	0.14	0.17	0.06	0.13	0.16	0.08	0.13	0.11	0.23	0.25	0.12	0.08	0.06	0.06	0.07	0.04	0.09	0.07
P ₂ O ₅	0.04	0.06	0.05	0.04	0.05	0.04	0.05	0.05	0.05	0.05	0.05	0.07	0.04	0.04	0.06	0.04	0.06	0.05
TiO ₂	0.62	0.68	0.33	0.62	0.48	0.10	0.51	0.29	0.46	0.50	0.41	0.56	0.35	0.39	0.55	0.26	0.41	0.27
PbO	0.01	ND	ND	ND	0.02	0.03	0.01	0.03	0.02	0.02	0.04	0.02	0.02	0.01	0.02	0.01	0.04	0.01
ZnO	0.01	ND	ND	ND	0.01	0.01	0.12	0.01	0.01	0.01	0.01	0.03	0.01	0.01	0.01	0.01	0.02	0.71
Total	93.78	94.95	79.15	93.90	87.95	78.55	92.10	80.90	91.17	84.43	83.14	84.63	82.64	88.12	93.73	81.01	84.31	78.64

Sample	YF04-37	YF04-38	YF04-39	YF04-40	YF04-41	YF04-42	YF04-43	YF04-44	YF04-45	YF04-46	YF04-47	YF04-48	YF04-49	YF04-50	YF04-51	YF04-52	YF04-54
Rock	Ore	Ore	Ore	Ore	Ore	Ore	Host	Ore	Ore	Ore	Ore	Ore	Ore	Ore	Ore	Ore	Host
Depth(m)	166.0	167.0	172.0	175.0	181.0	189.0	195.0	198.0	203.0	210.0	211.0	214.0	215.0	216.0	223.0	224.0	226.0
S(%)	25.60	25.12	41.40	23.28	10.56	10.72	1.62	33.16	30.16	25.24	27.92	11.36	14.60	1.44	10.04	12.76	0.60
C org(%)	1.06	0.63	0.59	0.94	0.29	0.27	1.42	0.70	0.68	0.51	0.69	1.09	0.76	1.53	0.14	0.19	0.00
Major oxides (wt. %)																	
SiO ₂	37.66	34.36	10.06	39.26	43.01	59.43	55.06	22.72	28.93	36.03	32.73	53.05	44.64	41.99	39.56	42.25	69.54
Al ₂ O ₃	5.98	7.62	0.95	6.27	18.24	9.23	11.34	4.23	5.32	8.14	5.76	9.17	7.69	3.42	16.30	12.10	15.96
Fe ₂ O _{3t}	31.96	31.30	53.26	29.16	12.98	13.58	2.50	41.45	37.91	31.69	35.81	15.25	20.26	2.69	18.53	28.87	2.40
K ₂ O	1.94	2.34	0.27	2.08	5.61	3.50	5.51	1.08	2.15	2.77	2.39	2.94	2.23	0.98	1.65	1.00	3.81
Na ₂ O	0.05	0.07	0.01	0.04	0.15	0.08	0.06	0.03	0.03	0.03	0.01	0.08	0.07	0.01	1.44	0.80	1.55
CaO	1.94	3.79	3.40	3.47	5.89	2.93	10.55	3.81	1.48	1.70	1.42	5.82	7.92	26.0	6.64	5.26	1.97
MgO	0.58	0.94	0.58	1.24	2.03	0.81	3.91	0.82	0.56	0.81	0.67	0.74	1.39	0.97	2.10	2.03	1.54
MnO	0.39	0.83	0.39	0.71	1.02	0.67	1.26	1.16	0.67	0.40	0.49	0.18	0.33	0.65	0.16	0.09	0.04
BaO	0.06	0.09	0.02	0.03	0.08	0.06	0.07	0.03	0.05	0.05	0.04	0.11	0.06	0.02	0.01	0.01	0.08
P ₂ O ₅	0.05	0.06	0.05	0.07	0.09	0.09	0.07	0.04	0.05	0.06	0.05	0.05	0.06	0.05	0.14	0.09	0.11
TiO ₂	0.25	0.37	0.05	0.31	0.89	0.51	0.41	0.17	0.22	0.39	0.23	0.43	0.31	0.13	0.48	0.45	0.48
PbO	0.03	0.03	0.06	0.03	0.02	0.02	ND	0.06	0.12	0.03	0.07	0.01	0.02	ND	0.04	0.03	ND
ZnO	0.03	0.11	0.02	0.26	1.01	0.15	ND	0.18	0.12	0.27	0.06	0.07	0.05	ND	5.45	0.03	ND
Total	80.92	81.91	69.11	82.93	91.02	91.06	90.74	75.78	77.61	82.37	79.73	87.90	85.03	76.90	92.50	93.01	97.48

Bblack shale from drill hole YF02, data cited from Qiu et al. (2018)												
Sample	YF02-03	YF02-04	YF02-05	YF02-06	YF02-07	YF02-08	YF02-09	YF02-10	YF02-11	YF02-12	YF02-13	YF02-14
Rock	Black shale	Black shale	Black shale	Black shale	Black shale	Black shale	Black shale	Black shale	Black shale	Black shale	Black shale	Black shale
Depth(m)	166.0	167.0	172.0	175.0	181.0	189.0	195.0	198.0	203.0	210.0	211.0	214.0
S(%)	2.74	3.53	2.80	1.59	2.54	3.29	3.75	3.18	3.25	1.94	0.69	1.60
C org(%)	1.02	1.28	1.44	1.12	1.83	2.03	0.36	1.91	1.02	1.42	2.89	1.26
Major oxides (wt. %)												
SiO ₂	59.89	63.78	53.65	62.01	75.69	69.82	60.87	63.85	60.02	70.14	82.79	68.25
Al ₂ O ₃	9.28	10.93	10.86	15.79	8.06	11.16	6.64	14.62	18.55	12.51	5.18	11.73
Fe ₂ O _{3t}	4.96	5.90	5.03	3.58	4.72	5.62	6.17	5.48	5.57	4.00	2.50	3.60
K ₂ O	2.38	2.83	2.75	4.35	1.87	3.03	1.00	4.38	5.51	3.48	1.31	3.31
Na ₂ O	0.09	0.10	0.17	0.21	0.09	0.09	0.03	0.12	0.13	0.10	0.04	0.09
CaO	8.75	5.51	11.66	3.85	1.83	1.42	10.89	1.78	1.01	2.06	1.33	3.60
MgO	1.73	0.92	1.17	1.43	1.10	1.41	3.34	1.43	1.52	1.34	0.89	1.88
MnO	0.06	0.03	0.12	0.08	0.05	0.06	0.25	0.06	0.02	0.04	0.04	0.09
BaO	0.62	0.77	0.69	0.12	0.04	0.06	0.02	0.13	0.11	0.08	0.06	0.09
P ₂ O ₅	0.09	0.08	0.05	0.06	0.04	0.07	0.05	0.07	0.06	0.08	0.11	0.05
TiO ₂	0.28	0.32	0.31	0.59	0.20	0.40	0.34	0.56	0.74	0.54	0.18	0.51

Table 2

Lead isotope ratios of Pyrite 1 and 2 determined by in-situ analyses of pyrite in the laminated ores.

	$^{206}\text{Pb}/^{204}\text{Pb}$	1σ	$^{207}\text{Pb}/^{204}\text{Pb}$	1σ	$^{208}\text{Pb}/^{204}\text{Pb}$	1σ
YF09-2PY1	18.195	0.020	15.708	0.018	38.576	0.044
YF09-2SP1	18.195	0.034	15.718	0.029	38.595	0.071
YF09-2PY2	18.225	0.009	15.718	0.029	38.628	0.023
YF09-2SP2	18.167	0.023	15.695	0.021	38.529	0.050
YF09-2Py	18.264	0.022	15.772	0.019	38.709	0.047
YF09-2Py4	18.241	0.036	15.753	0.030	38.608	0.072
YF09-2PY3	18.167	0.154	15.718	0.134	38.512	0.328
YF09-2PY5	18.320	0.040	15.832	0.035	38.816	0.084
YF44-PY1	18.199	0.031	15.722	0.027	38.568	0.066
YF44-PY2	18.160	0.101	15.686	0.086	38.494	0.213
YF44-PY3	18.097	0.049	15.636	0.042	38.356	0.103
YF44-PY5	18.216	0.002	15.724	0.002	38.599	0.004
YF44-PY6	18.224	0.007	15.727	0.006	38.612	0.015
YF44-PY7	18.216	0.002	15.724	0.002	38.599	0.004
YF46-PY1	18.260	0.007	15.775	0.007	38.749	0.018
YF46-PY2	18.216	0.012	15.731	0.010	38.638	0.026
YF46-PY3	18.224	0.012	15.751	0.012	38.687	0.031
YF46-PY4	18.253	0.007	15.766	0.006	38.721	0.017
YF46-PY5	18.241	0.014	15.768	0.014	38.724	0.038
YF46-PY6	18.222	0.010	15.730	0.009	38.619	0.024
YF46-PY7	18.250	0.016	15.770	0.014	38.636	0.055
YF10-PY2	18.154	0.005	15.697	0.005	38.566	0.015
YF10-PO1	18.108	0.008	15.665	0.007	38.442	0.019
YF10-PY3	18.139	0.008	15.698	0.008	38.538	0.028
YF10-PY4	18.142	0.007	15.698	0.006	38.513	0.015
YF10-PY5	18.124	0.022	15.685	0.019	38.491	0.047
YF10-PY6	18.050	0.035	15.617	0.031	38.335	0.074
YF10-PO7	18.110	0.025	15.680	0.021	38.462	0.052
YF10-PY8	18.153	0.039	15.704	0.035	38.559	0.085
YF258-PO1	18.205	0.023	15.700	0.020	38.558	0.048
YF258-PY2	18.272	0.046	15.779	0.041	38.734	0.099
YF258-PY3	18.203	0.006	15.714	0.005	38.580	0.013
YF258-PY4	18.210	0.004	15.724	0.004	38.620	0.009

YF258-PY5	18.161	0.042	15.687	0.036	38.516	0.089
YF258-PY6	18.208	0.008	15.715	0.007	38.597	0.018
YF52-PY2	17.997	0.014	15.673	0.013	38.089	0.038
YF52-PY3	18.051	0.034	15.699	0.030	38.297	0.073
YF52-PY4	18.004	0.019	15.672	0.017	38.408	0.042
YF52-PY5	17.967	0.049	15.666	0.046	38.364	0.110
YF52-PY6	18.000	0.009	15.660	0.008	38.370	0.019
YF32-PY2	18.167	0.006	15.711	0.006	38.565	0.016
YF32-PY3	18.234	0.016	15.770	0.014	38.683	0.035
YF32-SP3	18.034	0.050	15.604	0.044	38.328	0.108
YF32-PY5	18.155	0.010	15.696	0.008	38.520	0.021
YF32-PY4	18.121	0.031	15.702	0.028	38.515	0.068
YF32-SP4	18.241	0.084	15.797	0.073	38.800	0.179
YF46-M1	18.253	0.011	15.777	0.010	38.716	0.027
YF10-M1	18.035	0.087	15.600	0.078	38.315	0.183
YF10-M3	18.113	0.051	15.615	0.043	38.338	0.104
YF10-M4	18.139	0.030	15.675	0.026	38.466	0.065
YF258-M1	18.220	0.028	15.701	0.023	38.589	0.058
YF258-M4	18.224	0.026	15.734	0.023	38.625	0.056
YF0426-01	18.370	0.046	15.791	0.039	38.830	0.097
YF0426-02	18.316	0.006	15.747	0.006	38.722	0.015
YF0426-03	18.343	0.034	15.746	0.028	38.731	0.071
YF0426-04	18.490	0.026	15.866	0.023	39.054	0.056
YF0426-05	18.404	0.028	15.806	0.025	38.915	0.060
YF0436-01	18.283	0.029	15.746	0.024	38.718	0.061
YF0436-02	18.270	0.033	15.721	0.029	38.633	0.070
YF0436-03	18.358	0.025	15.778	0.022	38.851	0.054
YF0436-04	18.298	0.037	15.762	0.032	38.751	0.079

Note: The samples were analysed by LA-MC-ICPMS at the State Key Laboratory of Continental Dynamics, Northwest University, Xi'an, China.

Table 3

Sulfur isotope ratios ($\delta^{34}\text{S}_{\text{V-CDT}}\text{‰}$) determined by in-situ analyses of pyrite grains from drill hole YF04 and drill hole YF02.

Samples from drill hole YF04					
Sample	Depth	Pyrite type	Spot no	$\delta^{34}\text{S}_{\text{V-CDT}}$ (‰)	2σ (‰)
YF0402	36.0	Py2	YF0402-1	-28.9	0.1
		Py1	YF0402-2	-26.7	0.1
		Py2	YF0402-3	-28.6	0.1
YF0403	37.6	Py2	YF0403-1	-27.5	0.1
		Py1	YF0403-2	-26.0	0.1
		Py1	YF0403-3	-29.2	0.1
YF0409	50.0	Py3	YF0409-1	5.7	0.0
		Py3	YF0409-2	5.1	0.1
		Py3	YF0409-3	5.2	0.0
		Py3	YF0409-4	-0.4	0.1
YF0410	54.0	Py3	YF0410-1	6.5	0.1
		Py3	YF0410-2	7.2	0.1
		Py3	YF0410-3	4.1	0.1
		Py3	YF0410-4	7.0	0.1
YF0411	56.0	Py3	YF0411-1	2.8	0.1
		Py3	YF0411-2	3.6	0.1
		Py3	YF0411-3	1.7	0.1
		Py3	YF0411-4	4.7	0.1
		Py3	YF0411-5	5.2	0.1
YF0412	59.0	Py3	YF0412-1	8.6	0.1
		Py3	YF0412-2	5.4	0.1
		Py3	YF0412-3	7.8	0.1
YF0413	62.5	Py3	YF0413-1	6.7	0.1
		Py3	YF0413-2	5.9	0.1
		Py3	YF0413-3	6.0	0.1
YF0414	68.0	Py3	YF0414-1	6.9	0.1
		Py3	YF0414-2	8.3	0.1
		Py3	YF0414-3	7.2	0.1
YF0415	70.0	Py3	YF0415-1	12.1	0.1
		Py3	YF0415-2	11.5	0.1
		Py3	YF0415-3	13.7	0.1
		Py3	YF0415-4	12.7	0.2
		Py3	YF0415-5	14.4	0.1
YF0416	77.0	Py3	YF0416-1	5.8	0.1
		Py3	YF0416-2	6.6	0.1
		Py3	YF0416-3	6.0	0.1

Samples from drill hole YF04					
Sample	Depth	Pyrite type	Spot no	$\delta^{34}\text{S}_{\text{V-CDT}}$ (‰)	2 σ (‰)
YF0417	81.0	Py3	YF0417-1	5.9	0.1
		Py3	YF0417-2	5.5	0.1
		Py3	YF0417-3	5.8	0.1
YF0418	85.0	Py3	YF0418-1	5.2	0.1
		Py3	YF0418-2	5.2	0.1
		Py3	YF0418-3	4.7	0.1
YF0419	90.5	Py1	YF0419-1	-19.6	0.1
		Py2	YF0419-2	-19.9	0.1
		Py1	YF0419-3	-19.7	0.1
YF0422	98.0	Py1 core	YF0422-1	-18.5	0.1
		Py1 rim	YF0422-2	-18.8	0.1
		Py1 core	YF0422-3	-18.9	0.1
		Py1 rim	YF0422-4	-19.3	0.1
		Py2	YF0422-5	-20.3	0.1
YF0423	100.0	Py2	YF0423-1	-19.4	0.1
		Py1	YF0423-2	-20.4	0.1
		Py2	YF0423-3	-18.8	0.1
YF0436	164.0	Py1 core	YF0436-1	-22.5	0.1
		Py2 rim	YF0436-2	-22.4	0.1
		Py2 core	YF0436-3	-22.4	0.1
		Py2 rim	YF0436-4	-22.5	0.1
		Py2	YF0436-5	-22.3	0.1
		Py1	YF0436-6	-22.5	0.1
YF0438	167.0	Py2	YF0438-1	-21.4	0.1
		Py1	YF0438-2	-21.8	0.1
		Py2	YF0438-3	-21.4	0.1
YF0443	195.0	Py1	YF0443-1	-26.0	0.1
		Py1	YF0443-2	-26.0	0.1
		Py2	YF0443-3	-25.8	0.1
YF0444	198.0	Py2	YF0444-1	-25.2	0.1
		Py1	YF0444-2	-25.1	0.1
		Py2	YF0444-3	-24.8	0.1
		Py1	YF0444-4	-24.8	0.1
YF0450	216.0	Py1	YF0450-1	-15.9	0.1
		Py1	YF0450-2	-17.7	0.1
		Py1	YF0450-3	-17.3	0.1

Samples from drill hole YF02					
Sample	Depth	Pyrite type	Spot no	$\delta^{34}\text{S}_{\text{V-CDT}}$ (‰)	2σ (‰)
YF0203	60.0	Py3	YF0203-1	4.0	0.1
		Py3	YF0203-2	4.7	0.1
		Py3	YF0203-3	15.8	0.2
		Py3	YF0203-4	3.8	0.1
YF0204	63.0	Py3	YF0204-1	12.2	0.5
		Py3	YF0204-2	18.6	0.5
		Py3	YF0204-3	42.9	0.1
YF0205	68.0	Py3	YF0205-1	25.3	0.2
		Py3	YF0205-2	-1.5	0.1
		Py3	YF0205-3	-1.4	0.1
YF0206	73.0	Py3	YF0206-1	2.9	0.1
		Py3	YF0206-2	2.7	0.1
		Py3	YF0206-3	1.7	0.1
YF0207	81.0	Py3	YF0207-1	15.6	0.1
		Py3	YF0207-2	16.1	0.1
		Py3	YF0207-3	15.3	0.1
YF0208	83.0	Py3	YF0208-1	11.2	0.0
		Py3	YF0208-2	11.9	0.1
		Py3	YF0208-3	11.5	0.1
YF0209	86.0	Py3	YF0209-1	3.4	0.1
		Py3	YF0209-2	3.1	0.1
		Py3	YF0209-3	2.8	0.1
YF0210	92.0	Py3	YF0210-1	11.0	0.1
		Py3	YF0210-2	11.0	0.1
		Py3	YF0210-3	11.7	0.1
YF0211	100.0	Py3	YF0211-1	3.0	0.1
		Py3	YF0211-2	3.3	0.1
		Py3	YF0211-3	2.8	0.1
		Py3	YF0211-4	2.4	0.1
YF0212	104.0	Py3	YF0212-1	5.4	0.1
		Py3	YF0212-2	5.2	0.1
		Py3	YF0212-3	5.1	0.1
		Py3	YF0212-4	5.2	0.1
YF0213	109.0	Py3	YF0213-1	12.0	0.1
		Py3	YF0213-2	12.2	0.1
		Py3	YF0213-3	12.0	0.1

Samples from drill hole YF02					
Sample	Depth	Pyrite type	Spot no	$\delta^{34}\text{S}_{\text{V-CDT}}$ (‰)	2σ (‰)
YF0214	113.0	Py3	YF0214-1	3.6	0.1
		Py3	YF0214-2	1.7	0.1
		Py3	YF0214-3	3.8	0.0
YF0215	120.0	Py2	YF0215-1	-25.3	0.1
		Py2	YF0215-3	-25.4	0.1
		Py1	YF0215-4	-25.6	0.1
YF0217	129.0	Py1	YF0217-2	-12.7	0.1
		Py1	YF0217-1	-13.1	0.1
YF0218	137.0	Py1	YF0218-1	-3.1	0.1
		Py1	YF0218-2	-3.0	0.1
YF0220	150.0	Py1	YF0220-1	-2.7	0.1
		Py1	YF0220-2	-3.1	0.1
YF0222	156.0	Py1	YF0222-1	10.7	0.2
		Py1	YF0222-2	9.8	0.1

Note: The samples were analysed by LA-MC-ICPMS at the State Key Laboratory of Continental Dynamics, Northwest University, Xi'an, China. Py1= *Pyrite 1*, Py2= *Pyrite 2*, Py3=*Pyrite 3*.

Table 4

In-situ sulfur isotopes data ($\delta^{34}\text{S}_{\text{V-CDT}}\text{‰}$) of pyrite from open pit.

Sample	Pyrite	Spot no	$\delta^{34}\text{S}_{\text{V-CDT}}\text{ (‰)}$	$2\sigma\text{ (‰)}$
YF09-2	Py1	YF09-2-py1	3.0	0.2
	Py2	YF09-2-py2	2.8	0.2
	Py2	YF09-2-py3	2.9	0.2
	Py2	YF09-2-py4	2.8	0.2
	Py1	YF09-2-py5	2.9	0.2
	Py1	YF09-2-py6	2.7	0.2
YF10-2	Py1	YF10-2-py1	-16.7	0.5
	Py1	YF10-2-py7	-16.4	0.2
	Py1	YF10-2-py2	-17.1	0.3
	Py1	YF10-2-py3	-17.0	0.1
	Py2	YF10-2-py4	-18.1	0.2
	Py2	YF10-2-py5	-18.4	0.1
	Py2	YF10-2-py6	-17.4	0.1
	Py2	YF10-2-py8	-17.5	0.2
YF25-8	Py1	YF25-8-py1	17.7	0.2
	Py2	YF25-8-py2	19.3	0.2
YF32	Py2	YF32-py2	18.9	0.2
	Py2	YF32-py3	18.5	0.1
	Py2	YF32-py4	18.5	0.2
	Py2	YF32-py5	20.5	0.2
YF44	Py2	YF44-py2	22.5	0.2
	Py2	YF44-py3	22.9	0.2
	Py2	YF44-py4	24.1	0.2
	Py2	YF44-py5	25.3	0.2
	Py2	YF44-py6	23.0	0.2
YF46-1	Py2	YF44-py7	25.1	0.2
	Py2	YF46-1-py1	-3.3	0.2
	Py1	YF46-1-py2	-3.6	0.2
	Py2	YF46-1-py3	-3.4	0.2
	Py2	YF46-1-py4	-3.1	0.1
	Py1	YF46-1-py5	-3.5	0.2
	Py1	YF46-1-py6	-3.4	0.2
	Py1	YF46-1-py7	-3.4	0.2
	Py2	YF46-1-py8	-3.3	0.2

Notes: Samples were measured by LA-MC-ICPMS at the laboratory of the Geological Survey of Finland. Py1= *Pyrite 1*, Py2= *Pyrite 2*.

Table 5

Sulfur isotope ratios ($\delta^{34}\text{S}_{\text{V-CDT}}(\text{‰})$) of pyrite separates from drill hole YF04 and the open pit. The uncertainty (2σ) of all the samples is $<0.2\text{‰}$.

Sample from the drill hole YF04				Sample from open pit		
Sample	Depth	Pyrite type	$\delta^{34}\text{S}_{\text{V-CDT}}(\text{‰})$	Sample	Pyrite type	$\delta^{34}\text{S}_{\text{V-CDT}}(\text{‰})$
YF04-1	35.4	Laminated pyrite	-28.7	13YF55	Laminated pyrite	6.0
YF04-4	38.2	Laminated pyrite	-28.5	13YF48	Laminated pyrite	-22.0
YF04-5	41.0	Laminated pyrite	-25.8	13YF52	Laminated pyrite	-28.1
YF04-6	43.5	Laminated pyrite	-26.5	13YF10-2	Laminated pyrite	-17.1
YF04-7	45.0	Laminated pyrite	-25.3	13YF41	Laminated pyrite	12.2
YF04-20	91.5	Laminated pyrite	-19.2	13YF29	Laminated pyrite	14.3
YF04-24	109.0	Laminated pyrite	-18.5	13YF05	Laminated pyrite	-26.3
YF04-25	113.0	Laminated pyrite	-20.6	13YF37	Laminated pyrite	-22.0
YF04-26	115.0	Laminated pyrite	-17.9	13YF15-3	Laminated pyrite	7.4
YF04-27	117.0	Laminated pyrite	-20.6	13YF33	Laminated pyrite	-26.3
YF04-28	121.0	Laminated pyrite	-18.8	13YF10-3	Laminated pyrite	-9.7
YF04-28	121.0	Laminated pyrite	-18.9	13YF23-1	Laminated pyrite	-28.3
YF04-29	124.0	Laminated pyrite	-19.8	13YF25-3	Laminated pyrite	-22.6
YF04-30	133.0	Laminated pyrite	-17.7	13YF25-7	Laminated pyrite	-4.0
YF04-31	136.0	Laminated pyrite	-22.3	13YF23-2	Laminated pyrite	-26.4
YF04-32	141.0	Laminated pyrite	-20.3	13YF25-8	Laminated pyrite	19.0
YF04-33	145.0	Laminated pyrite	-18.8	13YF19-1	Laminated pyrite	18.3
YF04-33B	149.0	Laminated pyrite	-19.9	13YF34	Laminated pyrite	-17.4
YF04-34	155.0	Laminated pyrite	-20.7	13YF27	Laminated pyrite	-27.3
YF04-35	157.0	Laminated pyrite	-20.3	13YF31	Laminated pyrite	-20.3
YF04-36	164.0	Laminated pyrite	-22.3	13YF21-1	Massive pyrite	8.1
YF04-37	166.0	Laminated pyrite	-24.0	13YF08	Massive pyrite	5.9
YF04-39	172.0	Laminated pyrite	-24.3	13YF21-3	Massive pyrite	-8.4
YF04-40	175.0	Laminated pyrite	-25.9	13YF9-3	Massive pyrite	-10.0
YF04-40	175.0	Laminated pyrite	-25.8	13YF46	Massive pyrite	3.1
YF04-41	181.0	Laminated pyrite	-24.2			
YF04-42	189.0	Laminated pyrite	-24.6			
YF04-45	203.0	Laminated pyrite	-25.9			
YF04-46	210.0	Laminated pyrite	-24.7			
YF04-47	211.0	Laminated pyrite	-24.8			
YF04-48	214.0	Laminated pyrite	-17.3			
YF04-49	215.0	Laminated pyrite	-18.3			
YF04-51	223.0	Laminated pyrite	-2.3			
YF04-52	224.0	Laminated pyrite	-1.9			
YF04-52	226.0	Laminated pyrite	-1.7			

Note: The samples were analysed by ICPMS at the State Key Lab of Environmental

Geochemistry, Institute of Geochemistry (Guiyang), Chinese Academy of Sciences.

Fig. 1

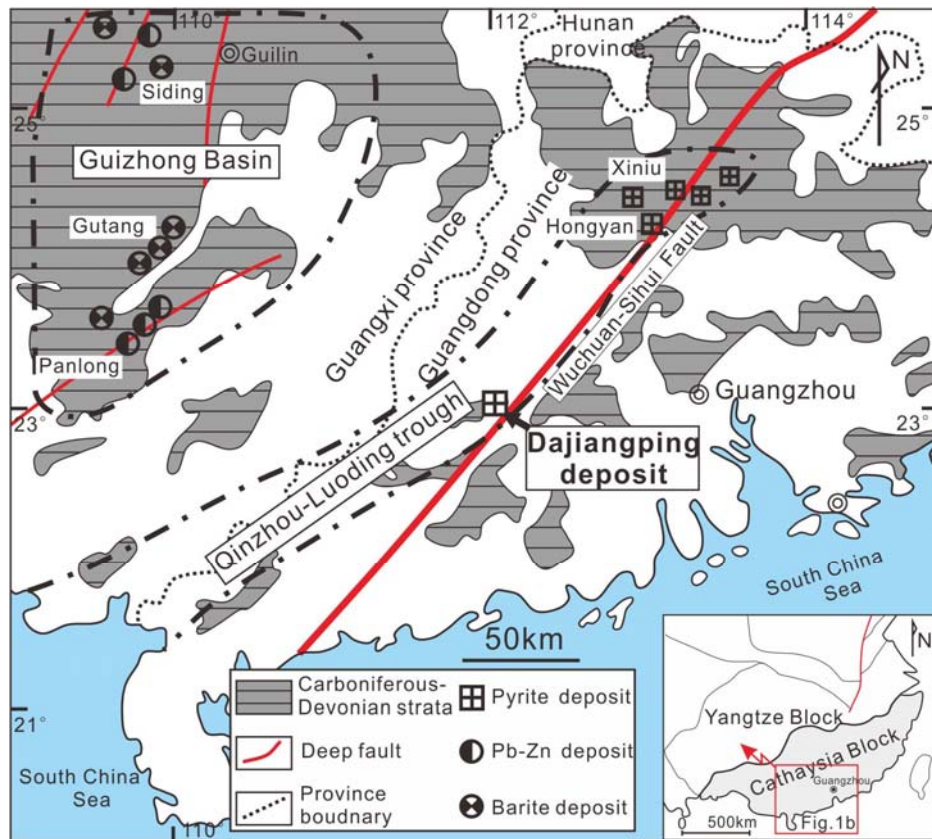


Fig.2

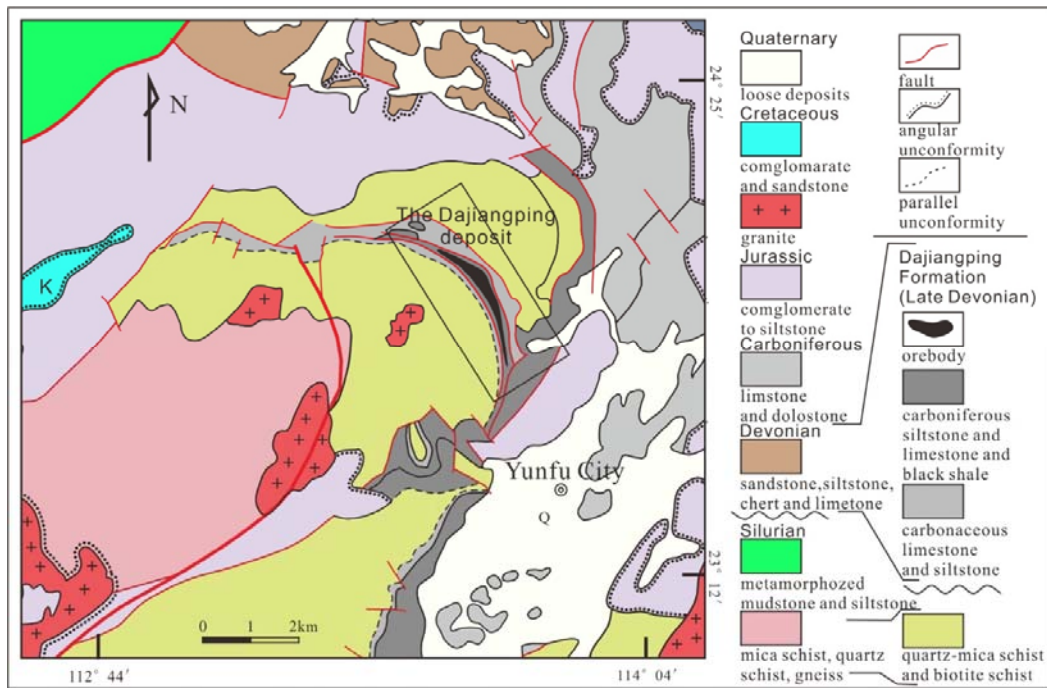


Fig.3

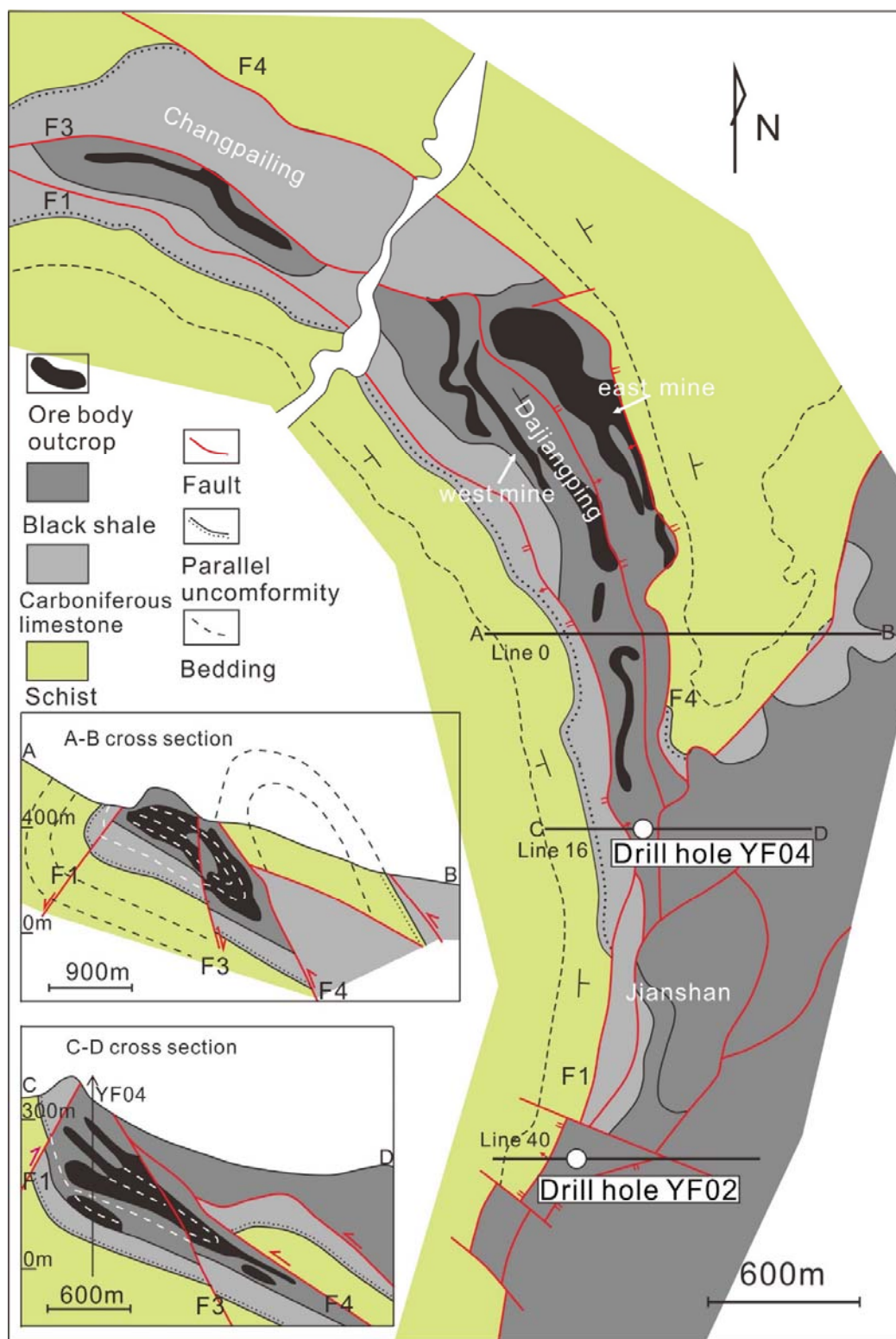


Fig.4

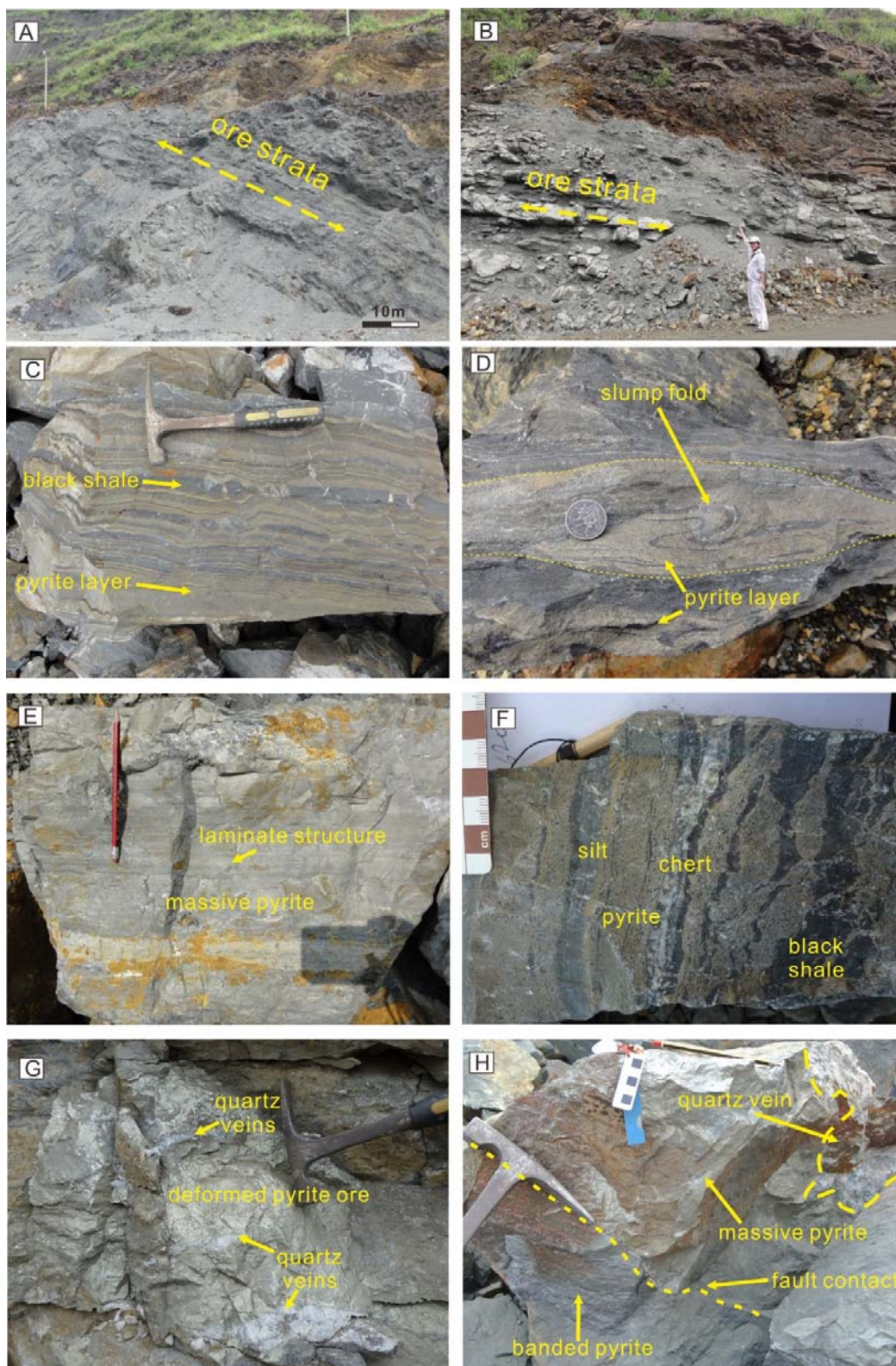


Fig.5

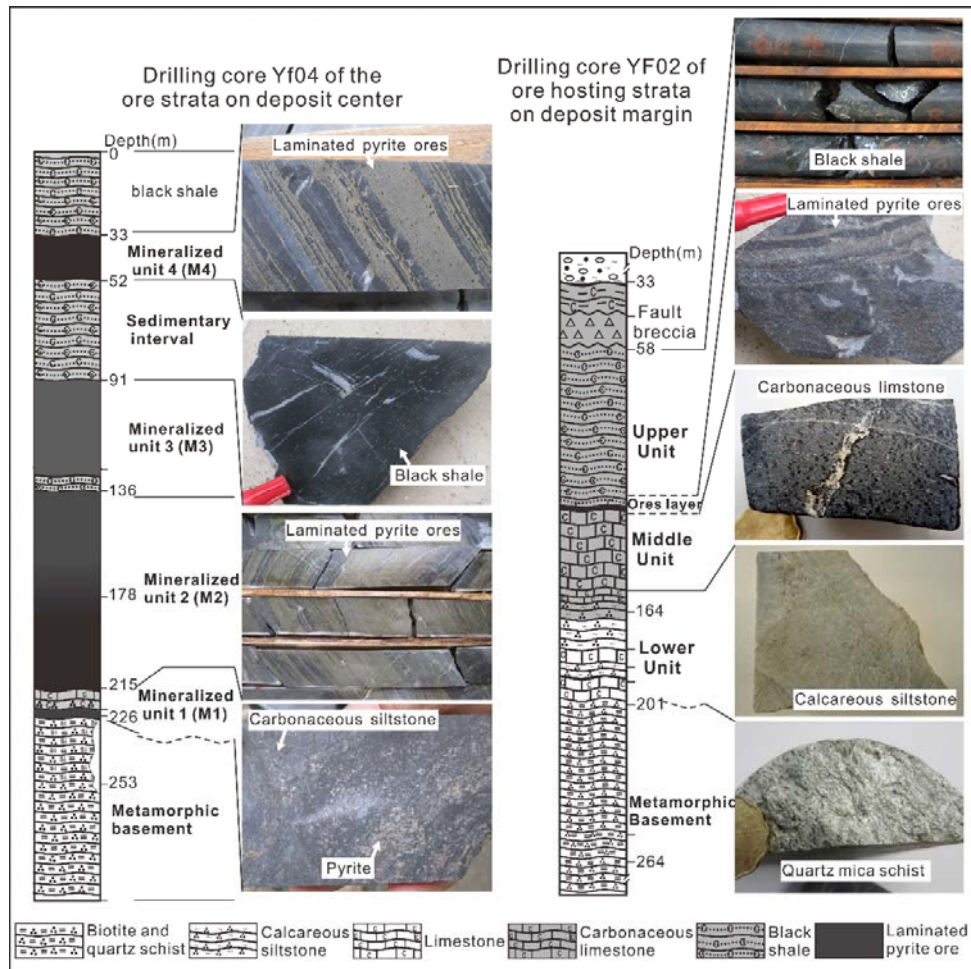


Fig. 6

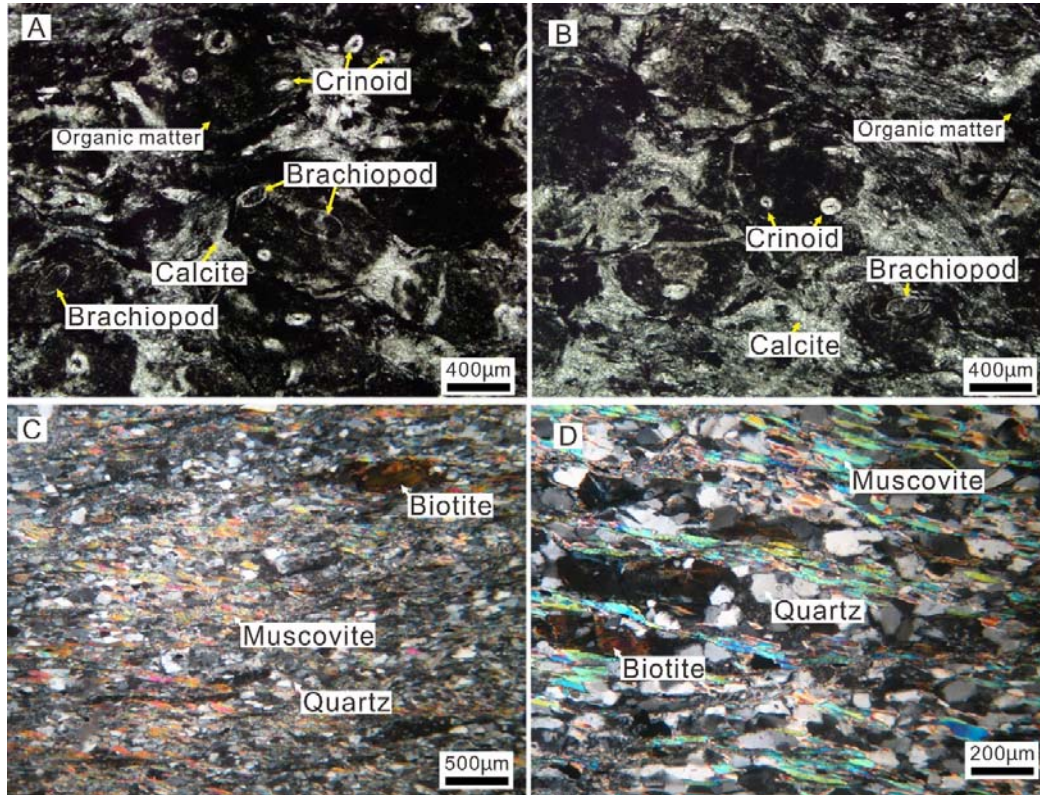


Fig.7

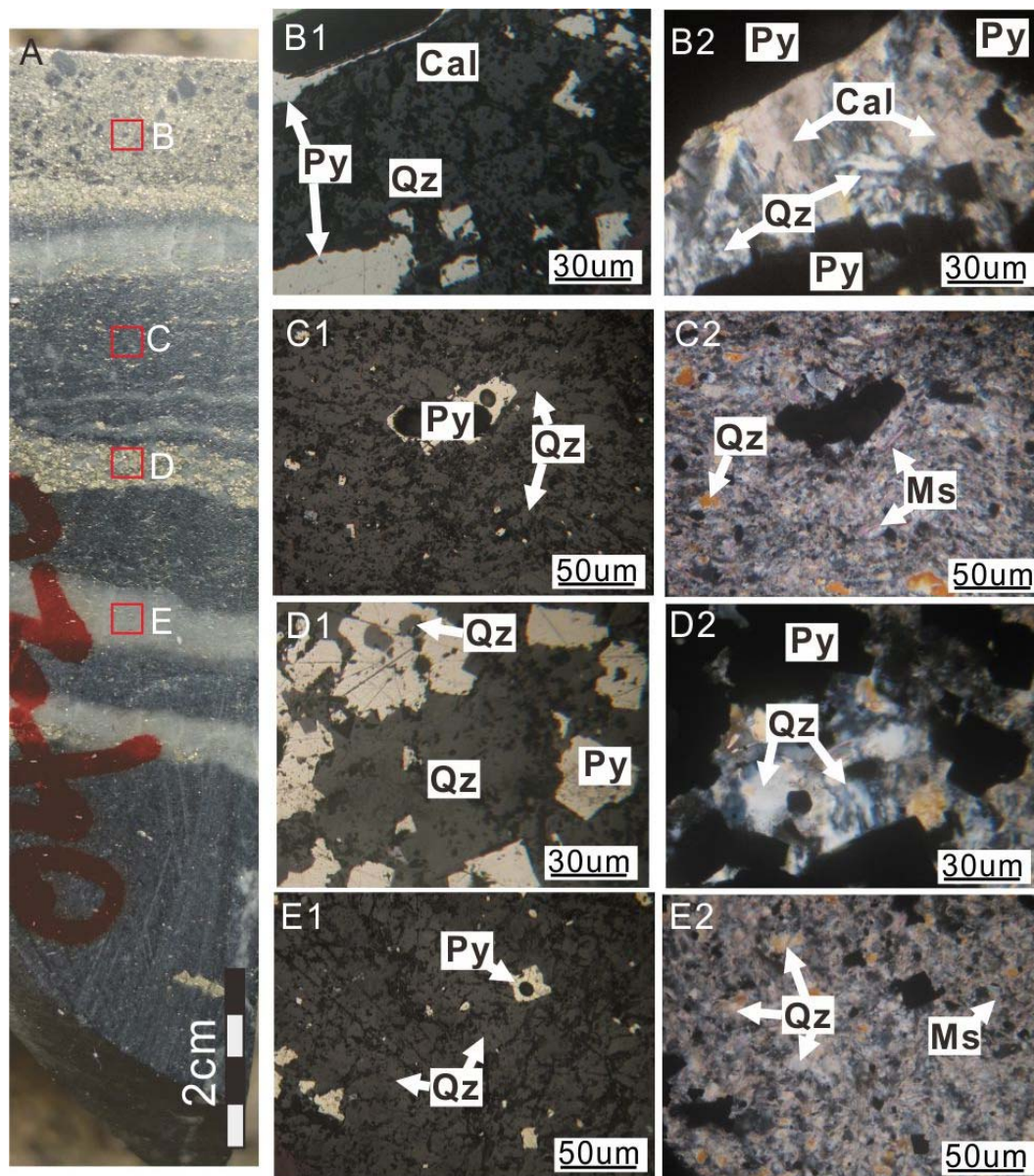


Fig.8

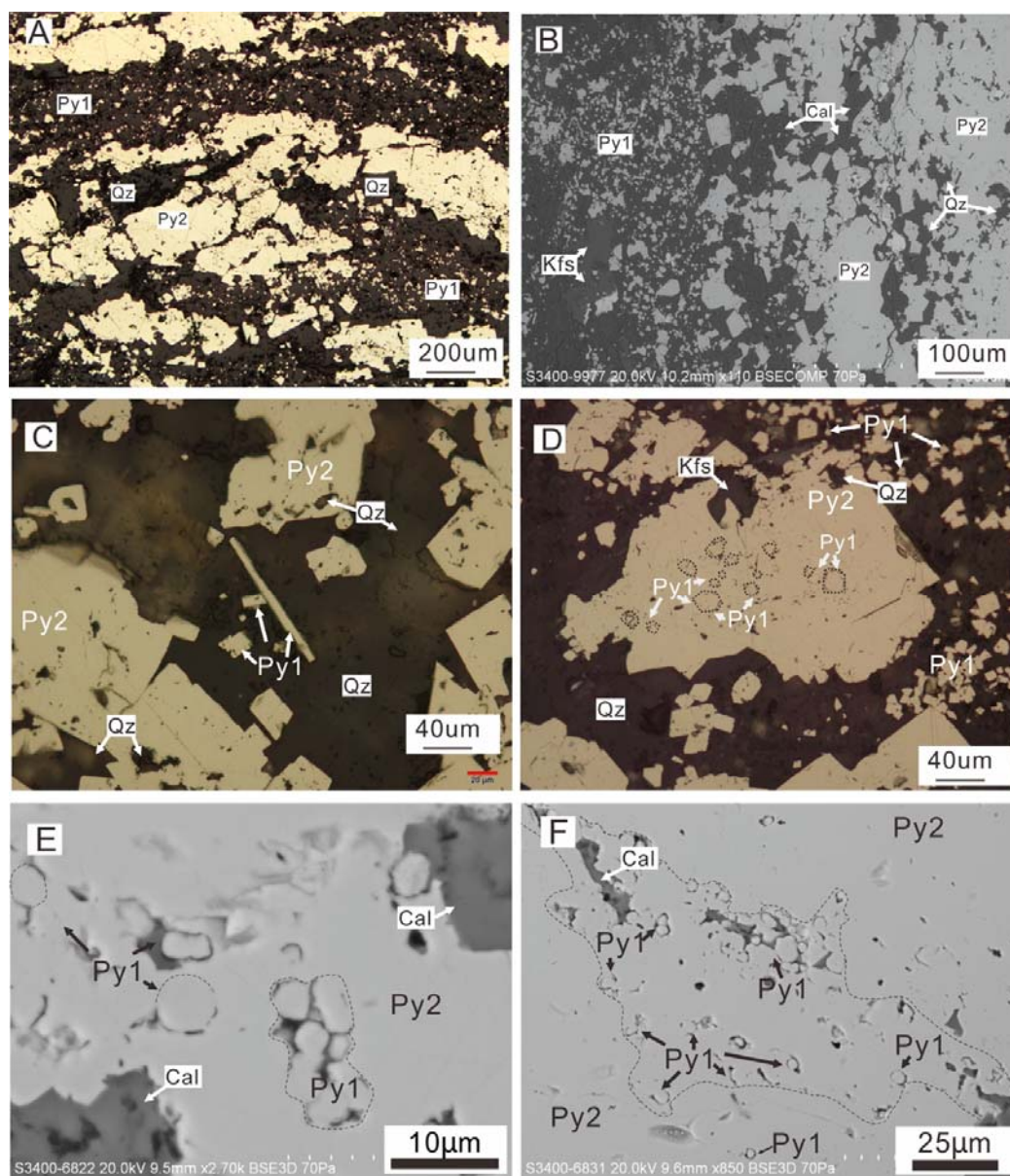


Fig.9

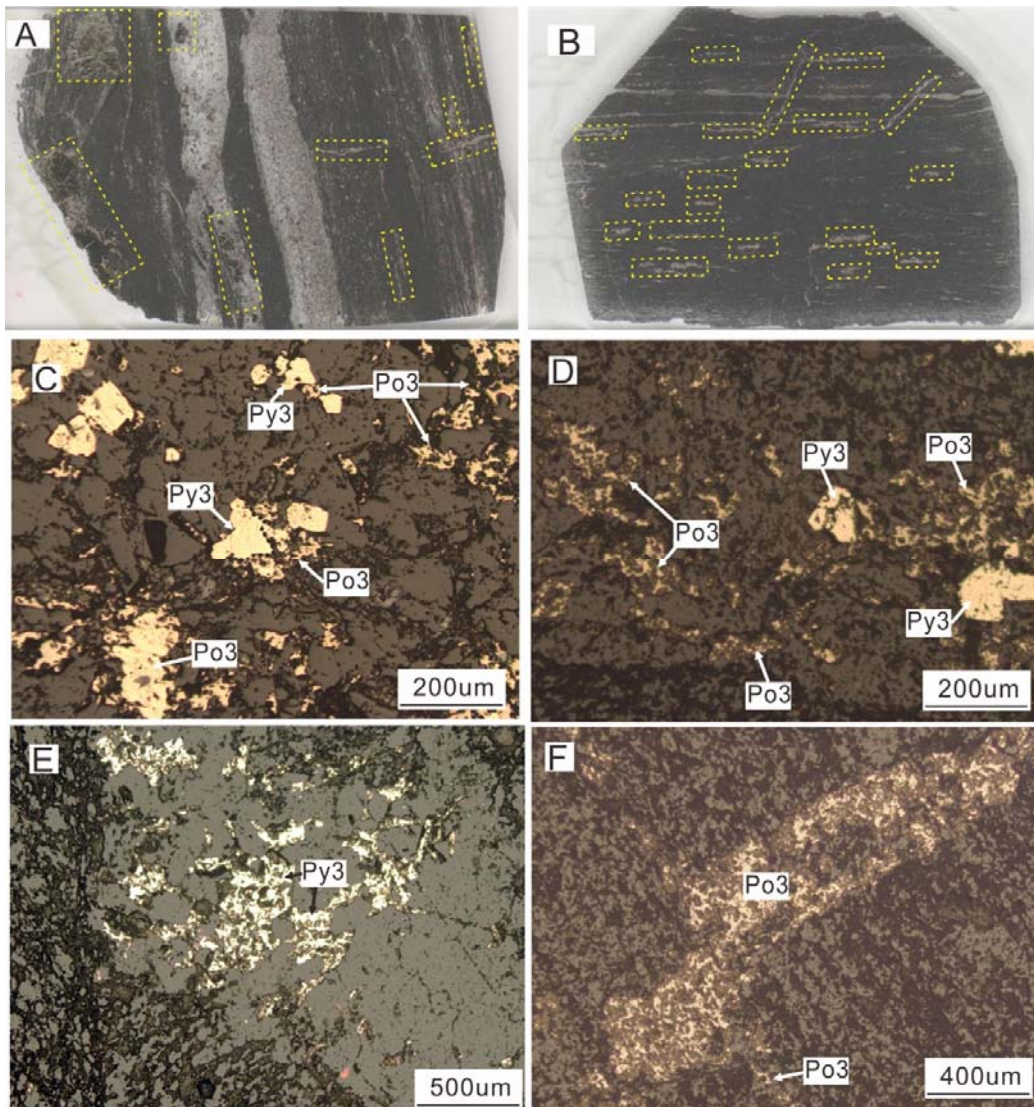


Fig.10

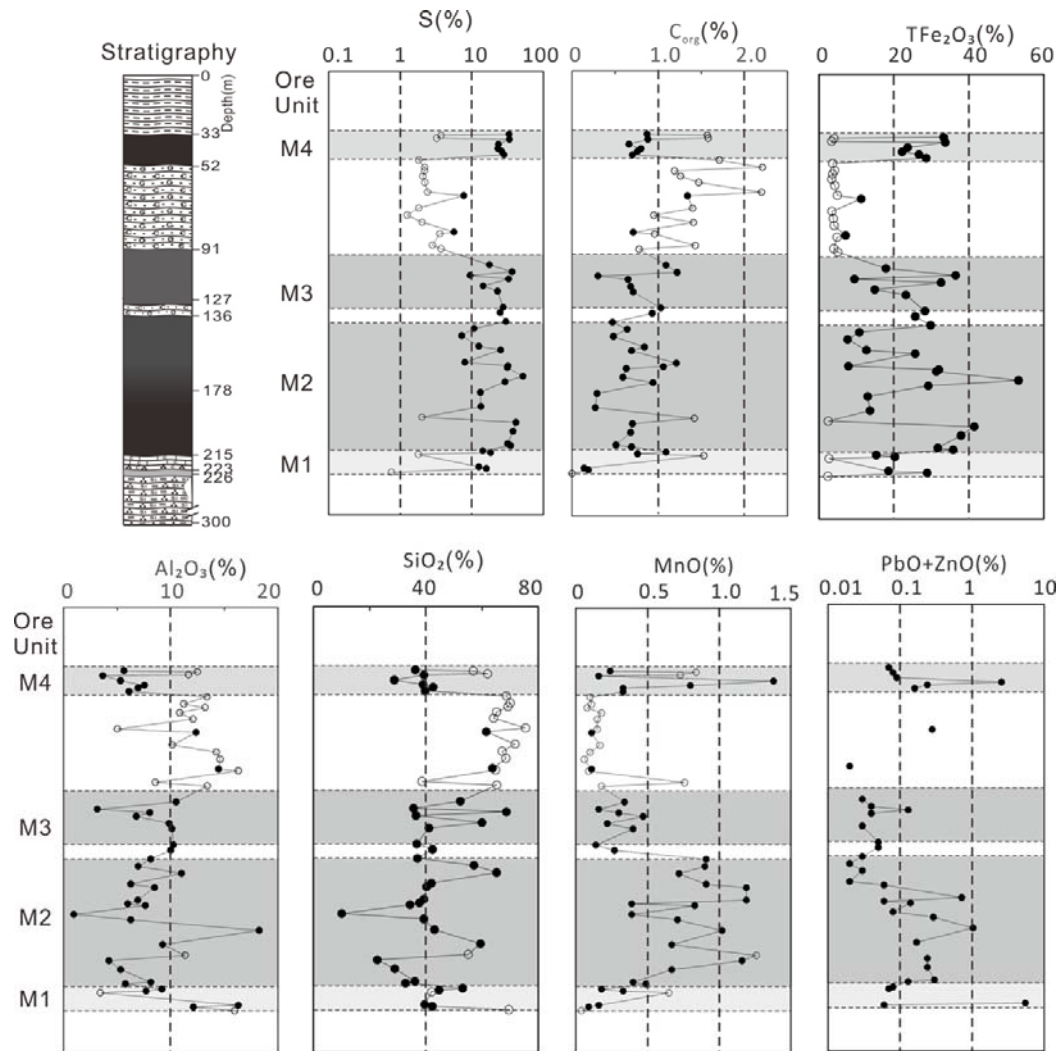


Fig.11

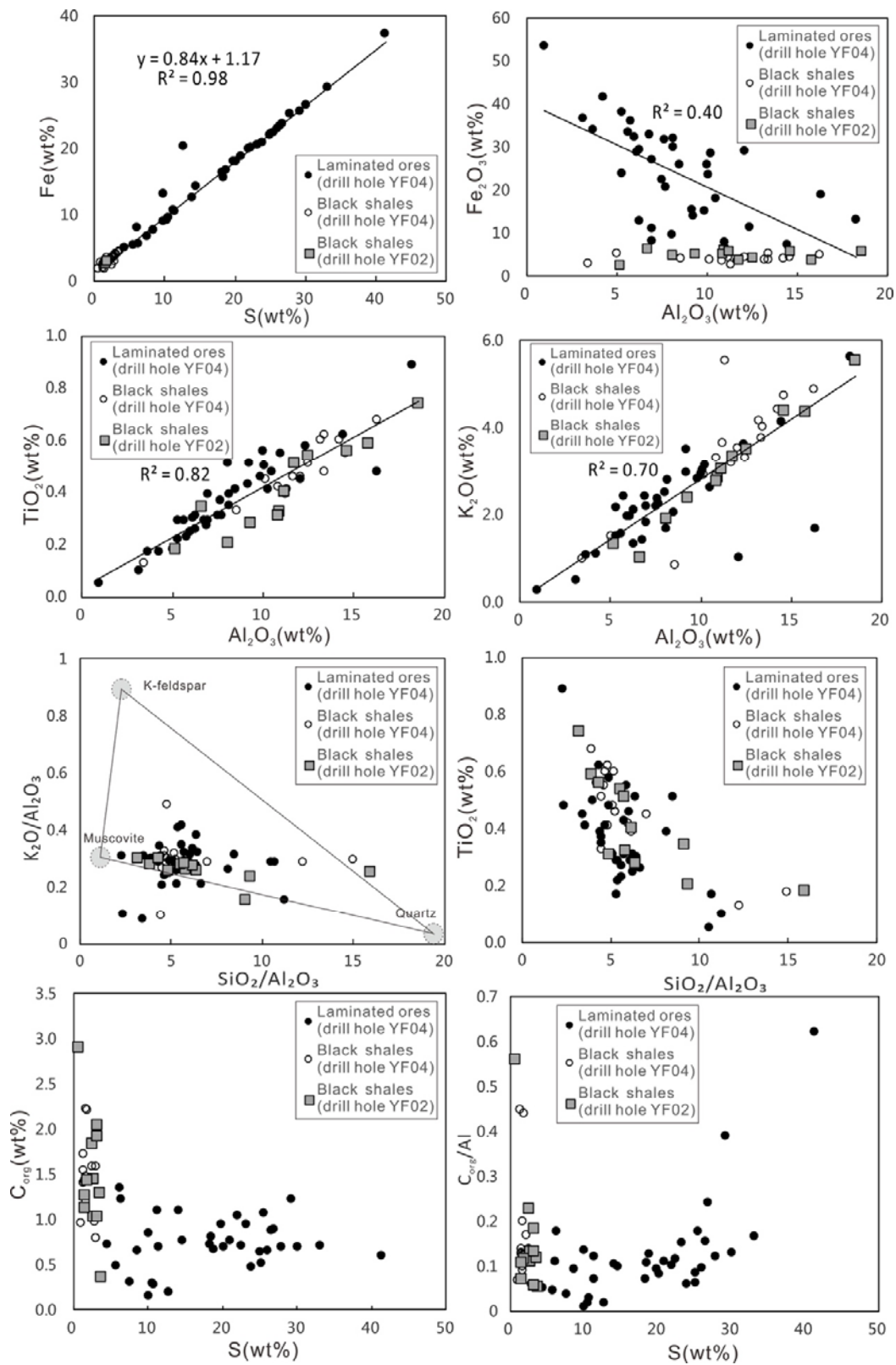


Fig.12

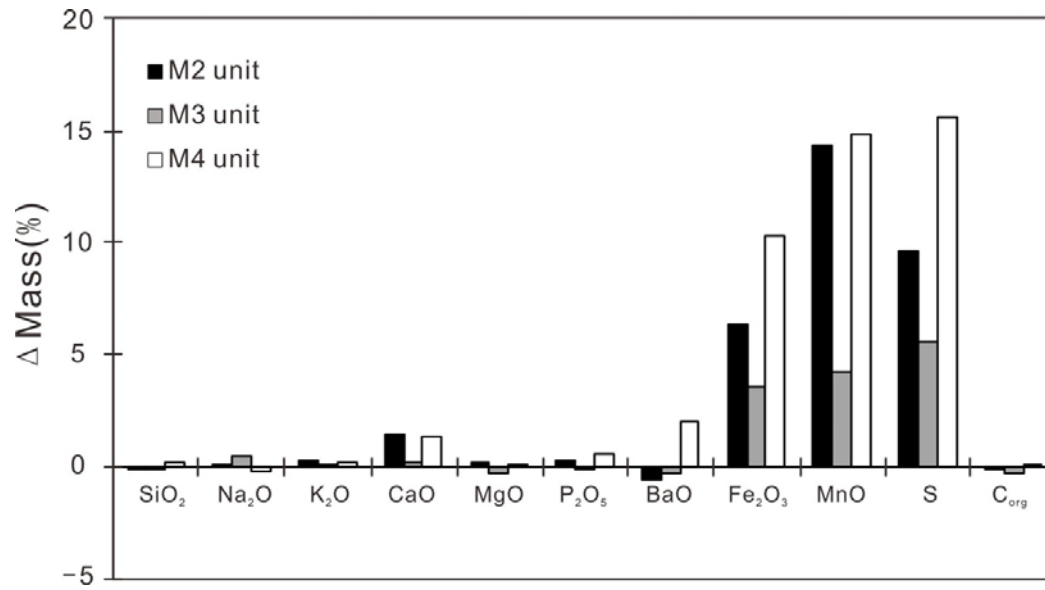


Fig.13

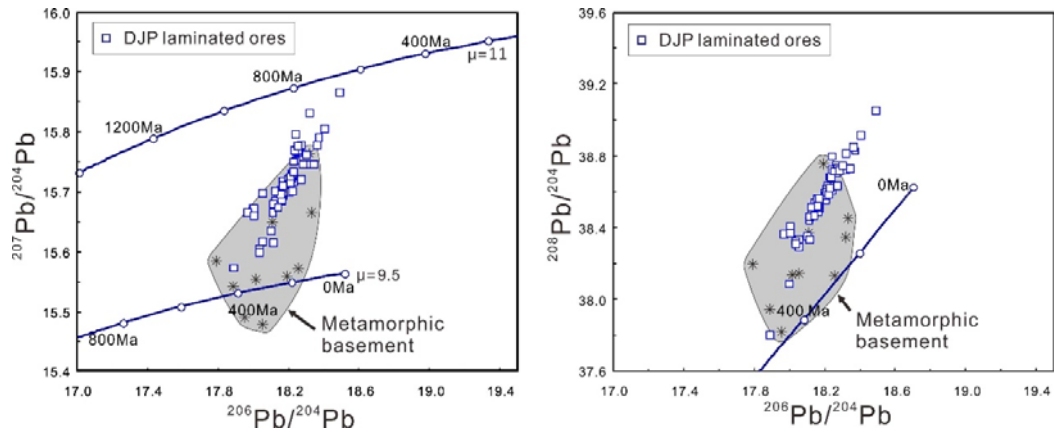


Fig.14

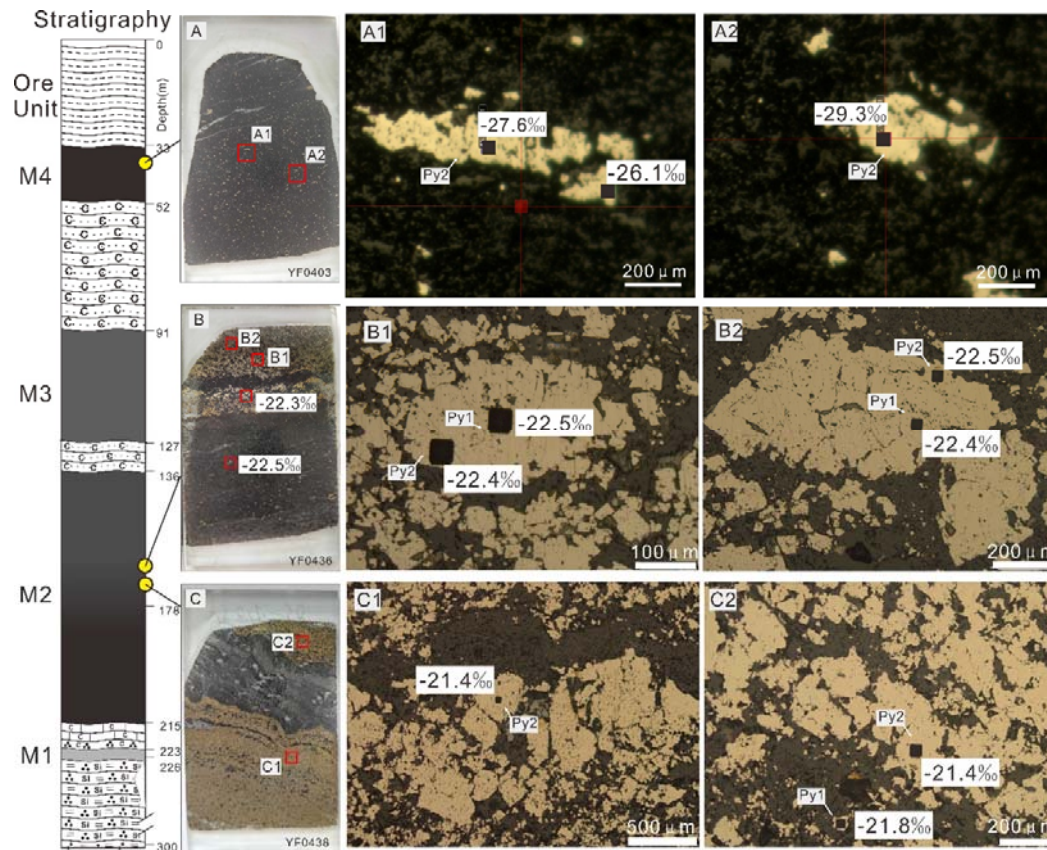


Fig.15

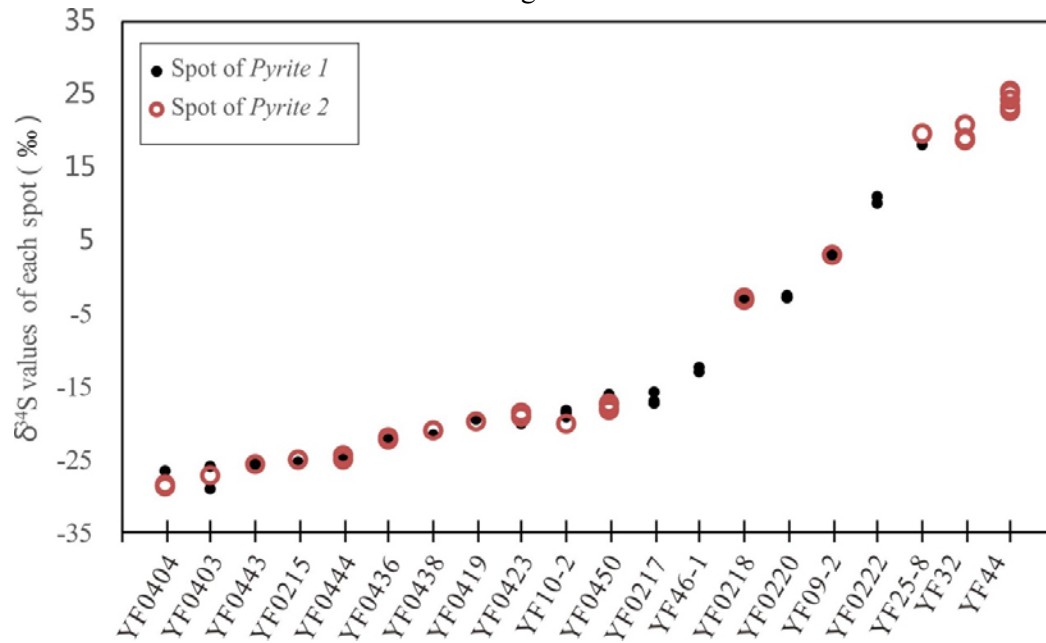


Fig.16

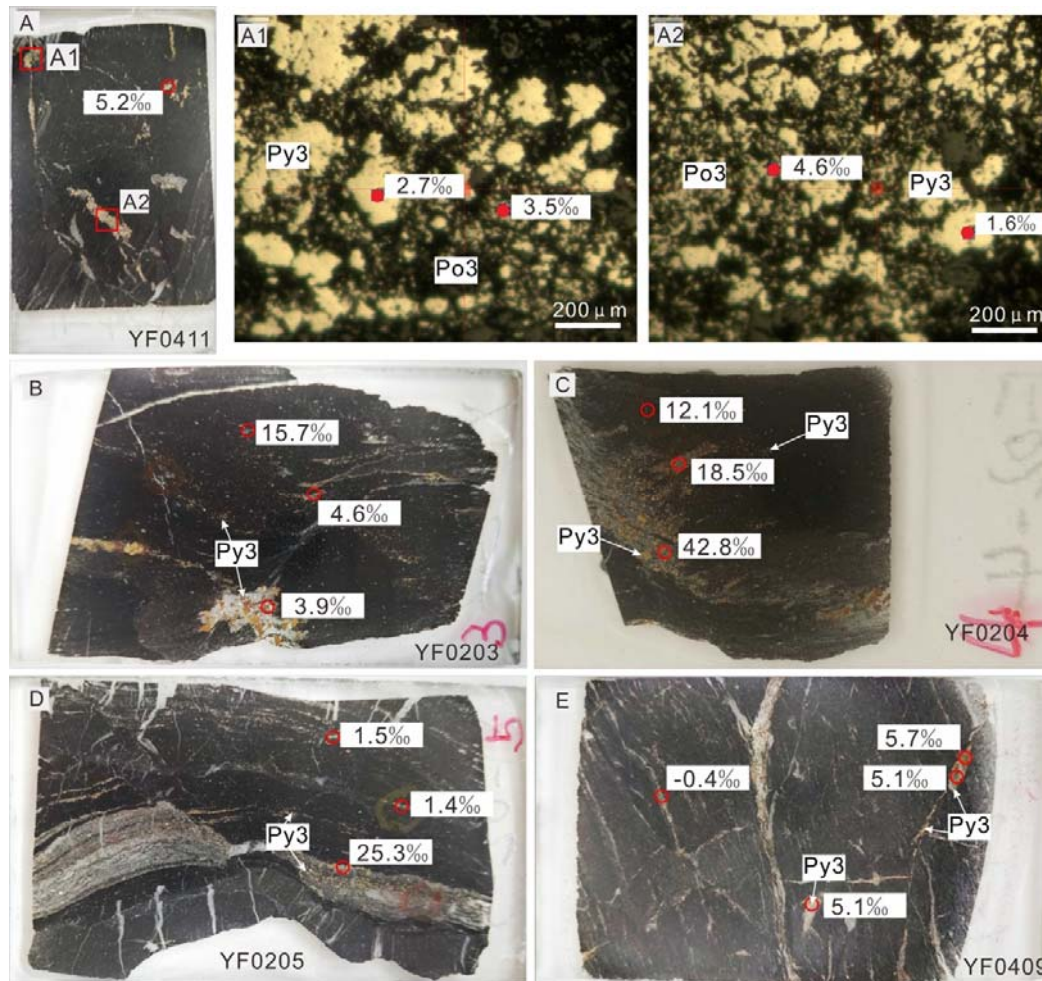


Fig.17

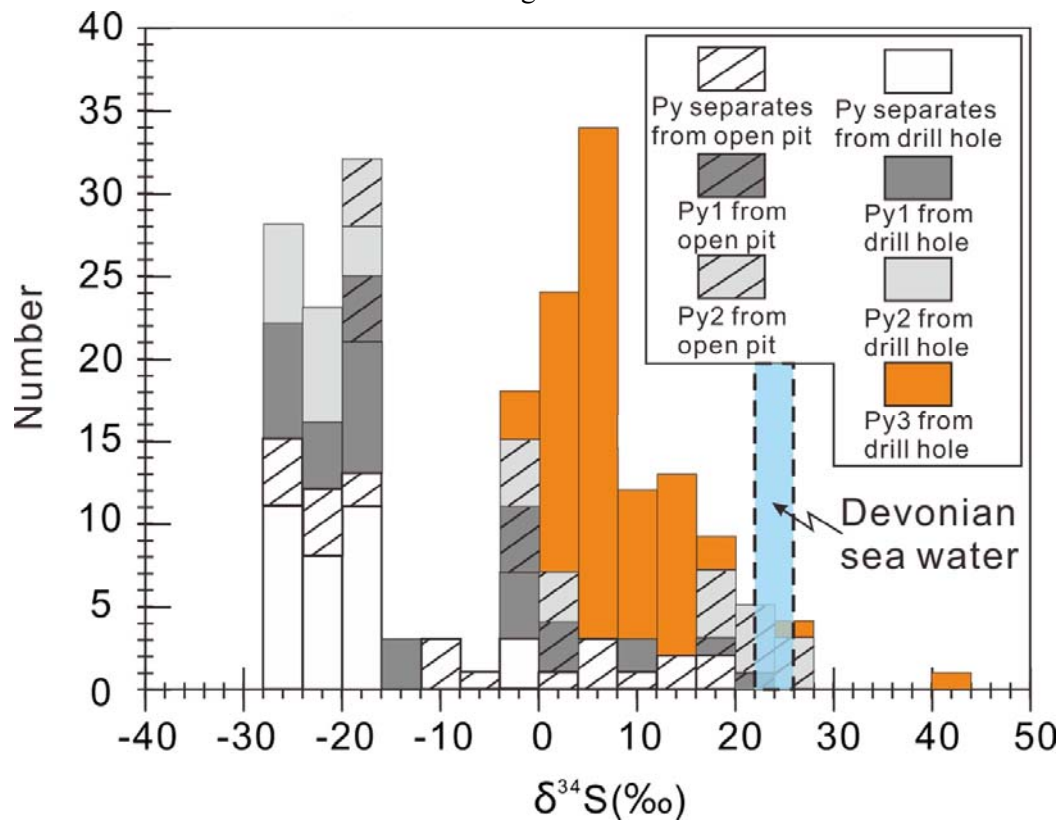


Fig.18

